

The High Latitude sNowfall Detection and Estimation aLgorithm for ATMS (HANDEL-ATMS): a new algorithm for the snowfall retrieval at high latitudes

Andrea Camplani¹, Daniele Casella¹, Paolo Sanò¹, Giulia Panegrossi¹

¹National Research Council of Italy, Institute of Atmospheric Sciences and Climate (CNR-ISAC), Via del Fosso del Cavaliere 100, 00133 Rome, Italy

Correspondence to: Andrea Camplani (Andrea.Camplani@artov.isac.cnr.it)

Abstract. ~~Snowfall detection and quantification are challenging tasks in the Earth system science field. Ground-based instruments have limited spatial coverage and are scarce or absent at high latitudes. Therefore, the development of satellite based snowfall retrieval methods is necessary for the global monitoring of snowfall. Passive Microwave (PMW) sensors can be exploited for snowfall quantification purposes because their measurements in the high frequency channels (> 80 GHz) respond to snowfall microphysics. However, the highly non-linear PMW multichannel response to snowfall, the weakness of snowfall signature and the contamination by the background surface emission/scattering signal make snowfall retrieval very difficult. This phenomenon is particularly evident at high latitudes, where light snowfall events in extremely cold and dry environmental conditions are predominant. Machine Learning (ML) techniques have been demonstrated to be very suitable to handle the complex PMW multichannel relationship to snowfall. Operational microwave sounders on near polar orbit satellites such as the Advanced Technology Microwave Sounder (ATMS), and the European MetOp-SG Microwave Sounder in the future, offer a very good coverage at high latitudes. Moreover, their wide range of channel frequencies (from 23 GHz to 190 GHz), allows for the dynamic radiometric characterization of the surface at the time of the overpass along with the exploitation of the high frequency channels for snowfall retrieval. The paper describes the High Latitude sNow Detection and Estimation aLgorithm for ATMS (HANDEL-ATMS), a new machine learning based snowfall retrieval algorithm developed specifically for high latitude environmental conditions and based on the ATMS observations.~~

~~HANDEL-ATMS is based on the use of an~~The High Latitude sNow Detection and Estimation aLgorithm for ATMS (HANDEL-ATMS) is a new machine learning (ML)-based snowfall retrieval algorithm for Advanced Technology Microwave Sounder (ATMS) observations that is developed specifically to detect and quantify high-latitude snowfall events that often form in cold, dry environments and produce light snowfall rates. ATMS and the future European MetOp-SG Microwave Sounder offer good high-latitude coverage and sufficient microwave channel diversity (23 to 190 GHz) that allows both surface radiometric properties to be dynamically characterized and the non-linear and sometimes subtle passive microwave response to falling snow to be detected. HANDEL-ATMS is based on a combined active-passive microwave observational dataset in the training phase, where each ATMS multichannel observation is associated with coincident (in time and space) CloudSat Cloud Profiling Radar (CPR) vertical snow ~~profile~~profiles and surface snowfall ~~rates~~rates. The main novelty of the approach is the radiometric characterization of the background surface (including snow-covered land and sea ice) at the time of the overpass to derive multi-channel surface emissivities and clear-sky contribution to be used in the snowfall retrieval process. The snowfall retrieval is based on four different artificial neural networks for snow water path (SWP) and surface snowfall rate (SSR) detection and ~~retrieval~~estimate. HANDEL-ATMS shows very good detection capabilities - POD = 0.83, FAR = 0.18, and HSS = 0.68 for the SSR detection module. Estimation error statistics show a good agreement with CPR snowfall products for SSR > 10⁻² mm h⁻¹ (RMSE = 0.08 mm h⁻¹, bias = 0.02 mm h⁻¹). The analysis of the results for an independent CPR dataset and of selected snowfall events evidence the unique capability of HANDEL-ATMS to detect and estimate SWP and SSR also in presence of extreme cold and dry environmental conditions typical of high latitudes.

1 Introduction

Snowfall retrieval is one important topic in the atmospheric science field. On a global scale, snowfall represents only 5 % of the total global precipitation but it is predominant above 60--70 ° N/S (see Levizzani et al, 2011). In recent years, several studies have highlighted the strong influence of global warming on snowfall distribution and regimes, especially at high latitudes (see Liu et al, 2009, Liu et al, 2012, Bintanja & Selten, 2014, Vihma et al,

49 2015). However, global snowfall quantification is a challenging topic in weather sciences. Ground-based
50 instruments such as raingauges or snowgauges provide only punctual measurements which can not fully capture
51 the spatial variability of precipitation phenomena: (*Kidd et al, 2017*); moreover, the variability of snowflake shape
52 and density ~~has a strong influence on their~~ strongly influences particle fall speed and ~~trajectories~~ trajectory and
53 therefore ~~reduces the~~ gauge-based ~~measurements~~ measurement accuracy of falling snow ~~result, especially~~
54 ~~compared~~ to be less accurate than for rain (~~see measurements~~ (*Skofronick-Jackson et al, 2015*). Weather radars
55 can provide areal measurements of precipitation - the rate estimation is based on the conversion of the measured
56 backscattered radiation to precipitating hydrometeors content - but such operation presents some technical
57 limitations (~~see~~ *Kidd & Huffman, 2011*). Finally, most of the regions where snowfall is predominant - such as
58 Greenland, Siberia, Canada, and Antarctica - are uninhabited or otherwise sparsely populated areas where weather
59 observation networks are very scarce or totally absent. Therefore, the development of satellite-based methods for
60 snowfall retrieval is necessary for global monitoring of snowfall. Passive Microwave (PMW) sensors ~~on~~
61 ~~board~~ onboard polar orbiting satellites can be exploited for snowfall detection purposes because the microwave
62 (MW) signal is directly responsive to the spatial distribution and microphysics properties of precipitation-sized
63 hydrometeors in the clouds; at the same time, the use of PMW sensors guarantees a high spatial coverage and high
64 temporal resolution (~~see~~ *Kidd & Huffman, 2011*).

65 PMW snowfall detection and quantification ~~is~~ are typically based on the ability to interpret the snowfall scattering
66 signature in the high-frequency channels (> 90 GHz), which respond more effectively to ice microphysics and
67 are less prone to surface effects than low-frequency channels, and to distinguish it from the clear-sky (surface
68 and atmosphere) contribution (e.g., *Panegrossi et al, 2017*). However, several factors make the PMW snowfall
69 signal ambiguous and the relationship between multichannel measurements and surface snowfall intensity highly
70 non-linear, especially in extremely cold/dry environmental conditions (~~see~~ *Panegrossi et al, 2022*). The snowfall
71 scattering signal is relatively weak and is highly dependent on the complex microphysical properties of snowflakes
72 (*Kim et al, 2008, Kulie et al, 2010, Kongoli et al, 2015*), it is often masked by supercooled liquid water emission
73 signal (*Wang et al, 2013, Battaglia & Delanoë Delanoë, 2013, Panegrossi et al, 2017, Rysman et al, 2018,*
74 *Battaglia & Panegrossi, 2020, Panegrossi et al, 2022*), and can be contaminated by the extremely variable
75 background surface emissivity (*Liu and Seo, 2013, Takkiri et al., 2019, Rahimi et al, 2017*), especially in cold
76 and dry conditions typical of the high latitude regions (*Camplani et al, 2021*). In this context, the availability of
77 the latest generation ~~microwave~~ MW radiometers - such as the conically-scanning radiometer GPM Microwave
78 Imager (GMI) and the cross-track scanning radiometer Advanced Technology Microwave Sensor (ATMS) -
79 whose channels cover a wide range of frequencies - offers new possibilities for global snowfall monitoring. The
80 multi-channel PMW observations can be used for both a dynamic radiometric characterization of the background
81 surface - using the low-frequency channels (< 90 GHz) - and for the detection and the estimation of the snowfall
82 using the high-frequency channels (> 90 GHz) (~~see~~ *Panegrossi et al, 2022*).

83 The PMW capability to characterize physically and radiometrically the background surface varies from sea to
84 land, especially for the identification of cold/frozen surfaces. For what concerns the ocean, sea ice detection using
85 PMW observations has been a well-documented topic in the remote sensing science field since the 70s. This is
86 due to the strong contrast between sea ice (≈ 0.9) and open water (≈ 0.5) emissivity values at the MW low-
87 frequency range (~ 19 GHz) (~~see~~ *Comiso, 1983*). Other studies highlighted the ability to discriminate between
88 different types of ice using a set of low-frequency window channels, because the differences between the
89 emissivities of the different types of sea ice increase with increasing frequency; in particular, at higher frequencies
90 (30-50 GHz) the contrast between the emissivity of “new” ice and “old” ice increases, with a decrease of the
91 emissivity at higher frequencies for “older” sea ice (~~see~~ *Comiso, 1983, Ulaby & Long, 2014*). Moreover, it has
92 been observed that the simultaneous presence of open water and sea ice causes a decrease in the low-frequency
93 channel emissivity; the observed emissivity can be considered as a linear combination of the emissivity spectra of
94 sea ice and open water (~~see~~ *Ulaby & Long, 2014*). For what concerns continental areas, the detection of snow-
95 covered land surfaces using MW measurements results to be more difficult. In dry conditions, a snowpack acts as
96 a volume scatterer; the scattering effect is dependent on the grain size and shape and ~~on~~ the depth of the snowpack
97 (~~see~~ *Clifford, 2010*). However, the presence of liquid water can mask the scattering signature (~~see~~ *Mätzler &*
98 *Hüppi, 1989*). At the same time, large areas of Greenland and Antarctica, while covered by dry snowpacks
99 throughout the year, do not show a significant difference between the two ATMS low-frequency channels.
100 Finally, some snow-free areas, such as rocky mountains and cold deserts, present a scattering signature very

101 similar to that of the snowpack (see *Grody & Basist, 1996*). Therefore, the detection of snow-covered areas is very
102 complex. A set of several tests, each of which identifies snowpacks characterized by different physical and
103 radiometric characteristics, may be used.

104 This paper describes the development of a machine learning-based algorithm for snowfall retrieval (the High
105 Latitude sNowfall Detection and Estimation aLgorithm for ATMS, HANDEL-ATMS), exploiting ATMS
106 radiometer multi-channel measurements and using the CloudSat Cloud Profiling Radar (CPR) snowfall products
107 as reference. The algorithm has been developed focusing on the typical conditions of high-latitude regions - low
108 humidity, low temperature, presence of snowpack on land or sea ice over ocean, and light snowfall intensity.

109 The main novelty of the approach is the exploitation of the ATMS wide range of channels (from 22 GHz to 183
110 GHz) to obtain the dynamic radiometric characterization of the background surface at the time of the overpass.
111 The derived surface emissivities are used to infer the clear-sky contribution to the measured [brightness](#)
112 [temperatures \(TBs\)](#) in the high-frequency channels in the snowfall retrieval process. This approach is similar to
113 the work of *Zhao and Weng, 2002*, for AMSU observations limited to non-scattering surfaces (i.e., ocean and
114 vegetated land), however the application to surfaces with a very complex and time-varying emissivity (such as
115 snow cover and sea ice) required a far-away more advanced algorithm taking advantage of machine learning
116 techniques. ~~Moreover, the algorithm is based on the exploitation of also exploits~~ an observational dataset ~~where~~
117 ~~each composed of~~ ATMS multichannel ~~observation is associated with observations and~~ coincident (in-time and
118 space) CloudSat CPR vertical snow ~~profile profiles~~ and surface snowfall ~~rates rates~~ (hereafter [the ATMS-CPR](#)
119 [coincidence coincident](#) dataset).

120 Several snowfall retrieval algorithms for cross-track scanning radiometers have evolved in the last 20 years
121 starting from the Advanced Microwave Sounder Unit-B (AMSU-B) (*Zhao and Weng, 2002, Kongoli et al, 2003,*
122 *Skofronick-Jackson et al, 2004, Noh et al, 2009, Liu and Seo 2013*), and Microwave Humidity Sounder (MHS)
123 (see *Liu & Seo, 2013, Edel et al, 2020*), and evolving to ATMS (*Kongoli et al, 2015, Meng et al, 2017, Kongoli*
124 *et al, 2018, You et al, 2022, Sanò et al, 2022*). Some of them are based on radiative transfer simulations of observed
125 snowfall events (*Kongoli et al, 2003, Skofronick-Jackson et al, 2004, Kim et al, 2008*), or on in-situ data (see
126 *Kongoli et al, 2015, Meng et al, 2017, Kongoli et al, 2018*), others on CPR observations (*Edel et al, 2020, You et*
127 *al, 2022, Sanò et al, 2022*), or a combination of them (*Noh et al, 2009, Liu & Seo, 2013*). In the last five years,
128 there has been an increasing use of machine learning (ML) approaches trained on CPR-based coincidence datasets.
129 These approaches have proven to be very effective for snowfall retrieval. On one side, ML techniques are suitable
130 to handle the complex, non-linear PMW multichannel response to snowfall (e.g., *Rysman et al, 2018, Edel et al,*
131 *2020, Sanò et al, 2022*). On the other hand, the use of CPR-based datasets overcomes some of the limitations
132 deriving from the use of cloud-radiation model simulations, which are particularly challenging for snowfall events.
133 However, some limitations of the radar product used as a reference and issues related to the spatial and temporal
134 matching between the CPR and the PMW radiometer measurements introduce some uncertainty. Moreover, the
135 [2-C-Snow-Profile \(2CSP\)](#) product is based on assumptions on snow microphysics, uses optimal estimation to
136 retrieve snow parameters, ~~and~~ uses a simplified radar reflectivity equation, and is affected by CloudSat CPR
137 limitations as outlined in *Battaglia & Panegrossi, 2020*.

138 For what concerns ATMS, the ML-based Snow retrieval ALgorithm fOr gpM-Cross Track (SLALOM-CT)
139 (*Sanò et al, 2022*) has been developed within the EUMETSAT Satellite Application Facility for Hydrology (H
140 SAF) in preparation for the launch of the EPS-SG Microwave Sounder (MWS). Similarly to HANDEL-ATMS, it
141 is trained on ~~an~~ ATMS-CPR coincidence dataset. SLALOM-CT is the evolution for cross-track scanning
142 radiometers of the Snow retrieval ALgorithm fOr GMI (SLALOM) (*Rysman et al, 2018, Rysman et al, 2019*)
143 which was the first ML algorithm for snowfall detection and retrieval for GMI trained and tested on GMI-CPR
144 coincident observations made available in the NASA GPM-CloudSat coincidence dataset (*Turk et al, 2021a*). One
145 of the novelties in the SLALOM (SLALOM-CT) approach is the use of the GMI (ATMS) low-frequency channels
146 to better constrain the snowfall retrieval to the characteristics of the surface at the time of the overpass (*Turk et*
147 *al, 2021b*). SLALOM-CT is based on a modular scheme, i.e., four separate modules are used for snowfall
148 detection, supercooled water layer detection, snow water path (SWP), and surface snowfall rate (SSR) estimate.
149 The predictor set is composed of the ATMS TBs and some environmental variables (~~T_{2m}~~ [2 meters Temperature -](#)
150 [T_{2m}, Total Precipitable Water -](#) TPW, and principal components derived from temperature and humidity profiles).
151 However, none of the algorithms mentioned here were tailored specifically to the extreme conditions typical of
152 high latitudes. The present work has the aim to develop an algorithm for snowfall detection and estimation by

153 exploiting the large frequency range typical of the last generation radiometers and to obtain a dynamic radiometric
154 characterization of the background surface at the time of the satellite overpass in order to highlight the complex
155 relationship between upwelling radiation and snowfall signature, which makes the detection very difficult in the
156 typical conditions of the high latitudes.

157 This article is organized as follows: Section 2 provides background information on ATMS and CPR, on the
158 methodology used to build the coincidence dataset, and on the machine learning approaches used to develop the
159 algorithm. In Section 3 the algorithm structure is described. In Section 4 the overall performance scores are
160 reported and analyzed; a case study is analyzed and a comparison with SLALOM-CT is reported. Section 5 is
161 dedicated to the summary of the main results and to the conclusions.

162 **2. Instruments and methods**

163 **2.1 Advanced Technology Microwave Sounder (ATMS)**

164 ATMS is a total power cross-track scanning radiometer within 52.7° off the nadir direction. It has a total of 22
165 channels with the first 16 channels primarily used for temperature sounding from the surface to about 1 hPa (45
166 km) and the remaining channels used for water vapor sounding in the troposphere from the surface to about 200
167 hPa (10 km), and for cloud properties and precipitation retrieval. There are two receiving antennas: one serving
168 channels 1–15 below 60 GHz, and the other for channels above 60 GHz. The beamwidth changes with frequency
169 and is 5.2° for channels 1–2 (23.8–31.4 GHz), 2.2° for channels 3–16 (50.3–57.29 and 88.2 GHz), and 1.1° for
170 channels 17–22 (165.5–183.3 GHz). The corresponding nadir resolutions are 74.78, 31.64, and 15.82 km,
171 respectively. The outmost field of view (FOV) sizes are $323.1 \text{ km} \times 141.8 \text{ km}$ (cross-track \times along-track), 136.7
172 $\text{km} \times 60.0 \text{ km}$, and $68.4 \text{ km} \times 30.0 \text{ km}$, respectively (see Weng *et al*, 2012). ATMS is currently carried by three
173 near-polar orbiting satellites, Suomi National Polar-orbiting Partnership (SNPP), NOAA-20, and NOAA-21
174 providing global coverage including polar regions. Each satellite revisiting time is equal to 12 hours at the equator,
175 but drops to 100 minutes over the polar regions, ensuring a very high temporal resolution for the research area of
176 interest in this work. Moreover, the operational nature of the mission guarantees observations for the next decades.
177 It is worth noticing that the polarization of ATMS channels is not defined as vertical or horizontal, but as “Quasi-
178 Vertical” or “Quasi-Horizontal”. The “Quasi” prefix is used to indicate that ATMS (and any other cross-track
179 scanner) measures vertical or horizontal polarization only when looking at nadir and a mixture of V and H
180 polarization for off-nadir scan angles.

181 **2.2 Cloud Profiling Radar (CPR)**

182 The CPR is a 94 GHz nadir-looking radar onboard CloudSat. CloudSat was launched on April 28, 2006; the W-
183 band (94 GHz) Cloud Profiling Radar (CPR) operations began on June 2, 2006. CPR has been acquiring the first-
184 ever continuous global time series of vertical cloud structures and vertical profiles of cloud liquid and ice water
185 content with a 485-m vertical resolution and a 1.4-km antenna 3-dB footprint. The reference CloudSat snowfall
186 product is the 2C-Snow-Profile (2CSP) product (Version 5 is used in this work). It provides estimates of snowfall
187 characteristics for each observed profile. In particular, it provides an estimate of the Snow Water Path (SWP), i.
188 e., the total snow water content integrated over the atmospheric column, and of the Surface Snowfall Rate (SSR)
189 (see Stephens *et al*, 2008). SWP is estimated also when there is no snowfall at the ground level, therefore, the
190 presence of SWP is not always linked to the SSR, especially in warmer near-surface conditions (see Wood &
191 L’Ecuyer, 2018). 2CSP has several limitations, such as the contamination of the signal in the lowest 1000 - 1500
192 m of the profile due to ground-clutter, the underestimation of the heavy snowfall, due to attenuation of the radar
193 signal in these conditions, and the limited temporal sampling (although it is higher in the polar regions), and the
194 day-only operation mode since 2011, which limits its use during the winter seasons (see Milani and Wood, 2021,
195 Panegrossi *et al*, 2022). However, 2CSP has been demonstrated to be more accurate than GPM Dual-frequency
196 Precipitation Radar (DPR) snowfall products (see Casella *et al*, 2017) and in good agreement with estimates
197 obtained by ground-based radars (e.g., Mroz *et al*, 2021), although it is affected by underestimation for medium-
198 heavy snowfall events. Moreover, the polar orbit and the W-band high sensitivity make CPR suitable for snowfall
199 monitoring at higher latitudes (as demonstrated in several studies, e.g., Kulie *et al*, 2016, Milani *et al*, 2018)
200 typically characterized by light/moderate intensity (Beranghi *et al*, 2016). These features appear to be an
201 advantage compared to the GPM-Core Observatory (GPM-CO), which provides observations only between 67°
202 N and 67° S, and to the K_u - and K_a -band DPR has low sensitivity and is not suitable to effectively detect light
203 snowfall events (Casella *et al*, 2017).

204 2.3 ATMS-CPR Coincidence Dataset

205 The present study is based on a coincidence dataset between CPR and ~~SNPP~~-ATMS observations between January
206 2014 and August 2016. The same dataset has been used for the development of SLALOM-CT (*Sanò et al, 2022*).
207 Each coincidence comes from observations from CloudSat CPR and ATMS ~~onboard SNPP~~—within a maximum
208 15-minute time window. In the period considered within the dataset, only the SNPP satellite was in orbit, so the
209 dataset is composed only of observations obtained from ATMS onboard this satellite. Moreover, the elements in
210 the dataset have been selected by removing all corrupted data and by applying an additional filter based on the
211 minimum distance between CPR and ATMS instantaneous field of view (IFOV) center ~~which~~ (22 km). The zonal
212 distribution of the coincidences is due to the orbital geometry of CloudSat and SNPP, which are both sun-
213 synchronous with a relatively small difference in the satellite height (i.e., about 689 km and 833 km for CloudSat
214 and SNPP respectively). Therefore, the coincidence dataset is built from longer orbit fragments (often semi-orbits)
215 and by a very large number of elements near the poles. There is an asymmetry in the CPR sampling between the
216 Northern and the Southern ~~hemisphere~~hemispheres that can be observed in the dataset due to the CPR daytime-
217 only mode operation since 2011, which influences mostly the acquisitions in the Southern Polar region (*Milani*
218 *and Wood, 2021*).

219 The database has been built considering the horizontal resolution of the high-frequency channels of ATMS. The
220 CPR snowfall product used as reference is the 2CSP (V5~~7~~) product. Some model-derived variables, specifically
221 the Total Precipitable Water (TPW), the 2-~~m~~meters Temperature (T_{2m}), the Skin Temperature, the freezing level
222 heightFreezing Level Height, and the temperature and humidity profiles, have been added to the dataset to be used
223 as ancillary parameters. Both 2D and 3D environmental variables have been obtained from the European Center
224 Medium Weather Forecast (ECMWF). In particular, they are obtained from the CPR ECMWF-AUX product
225 where the set of ancillary ECMWF atmospheric state variable data is associated with each CloudSat CPR bin (the
226 product is described by *Partain, 2022*). Moreover, a cloud-cover fraction index, which indicates the fraction of
227 CPR observations where cloud is observed on the total CPR observations within each ATMS pixel, is added to
228 the dataset.

229 Information about the presence of supercooled water is added into the coincidence dataset to be used towards the
230 correct interpretation of the snowfall signal in presence of supercooled water layers. ~~The~~ supercooled water
231 information has been extracted from the DARDAR product (see DARDAR, *Delanoë & Hogan, 2010*). DARDAR,
232 which stands for raDAR+LiDAR, combines CPR radar and Cloud-Aerosol Lidar with Orthogonal Polarization
233 (CALIOP) lidar observations, onboard Cloud-Aerosol Lidar and Infrared Pathfinder Satellite Observations
234 (CALIPSO) satellite, and estimates both the cloud water phase and the ice water content and ice particle effective
235 radius (see *Battaglia & Delanoë, 2013, Ceccaldi et al, 2013*). In particular, the coincidence dataset includes an
236 index indicating the presence of supercooled cloud liquid water within each ATMS pixel, calculated as the fraction
237 of DARDAR observations where supercooled water within and on the top of the cloud is observed to the total
238 DARDAR observations within each pixel.

239 The association of ATMS TBs and CPR products has been done by averaging the CPR snow products with a
240 Gaussian function approximating the ATMS high-frequency antenna pattern (varying with the scan angle). It is
241 worth noting, however, that the ATMS IFOV is under-sampled by the narrow swath of the CPR (see *Sanò et al,*
242 *2022* for details). Moreover, it is worth noting that CPR 2CSP-~~product~~ limitations for snowfall detection and
243 estimation (see Section 2.2) might affect the ATMS-based snowfall estimates.

244 In this work, the dataset has been filtered based on humidity (TPW < 10 mm), temperature (T_{2m} < 280 K), and
245 elevation conditions (the working limits of the PESCA algorithm, see *Camplani et al, 2021*) leading to a good
246 representation of the higher latitudes with 80 % of the dataset elements located above 60°N/S. The dataset is made
247 of $2,14 \cdot 10^6$ elements, including $1,07 \cdot 10^6$ elements with falling snow (2CSP SWP > 0 kg m⁻²) and $9,99 \cdot 10^5$ with
248 snowfall at the surface (2CSP SSR > 0 mm h⁻¹). The training and test phases have been conducted by splitting
249 randomly the dataset, with 1/3 of the elements in the training and 2/3 of the elements in the test dataset.

250 2.4 Machine Learning ~~approaches~~Approaches

251 The algorithm is based on different machine-learning (ML) techniques. Moreover, clustering techniques have
252 been used to characterize the background surface from a radiometric point of view ~~the background surface~~. In
253 particular, an unsupervised clustering technique has been used to identify emissivity clusters with small internal
254 variability, and a supervised clustering technique has been used to identify an emissivity spectrum based on other
255 parameters.

256 2.4.1 Artificial Neural Networks

257 The HANDEL-ATMS snowfall detection and estimation modules have been developed using feedforward
258 multilayer neural network architectures, i.e., a neural network architecture where the neurons are arranged in
259 layers. This architecture, which is defined by the number of layers, the number of neurons for each layer, and the
260 transfer function of each neuron, has to be designed beforehand. The weights of connection links and the bias
261 values for each layer are estimated with a training process, based on the Levenberg–Marquardt algorithm (see
262 Sanò et al, 2015). The specific ~~networks architecture~~ network architectures and the training and optimization
263 procedure of the HANDEL-ATMS algorithm are described in detail in section 3.2.

264 2.4.2 Self Organizing Maps

265 The unsupervised clustering method used for the background surface classification is the Self Organizing Map
266 (SOM) method (see Faussett, 2006, Kohonen, 2012). The characteristic of this method is that classes that are close
267 to each other from a topological point of view can be considered similar also from a physical and radiometric
268 point of view (see Munchak et al, 2020). SOMs have been used in previous studies for the classification of the
269 background surface by creating clusters based on emissivity values (see Prigent et al, 2001, Cordisco et al, 2006,
270 Prigent et al, 2008, Munchak et al, 2020).

271 2.4.3 Linear Discriminant Analysis

272 Several supervised clustering methods have been tested in this study, such as the linear discriminant analysis, the
273 quadratic discriminant analysis, the classification tree, and the nearest neighbor method. The final choice came
274 down to linear discriminant analysis (LDA, see Hastie et al, 2009) because this method guarantees satisfactory
275 accuracy in the results with a difference between the performances of the training and the test phase which is not
276 too significant, and a computational effort which is not too high.

277 3 Algorithm description

278 The configuration of the HANDEL-ATMS is summarized in the Flowchart in Figure 1. The process begins with
279 the classification of the background surface using the PMW Empirical cold Surface Classification Algorithm
280 (PESCA, see Camplani et al, 2021); then, the surface emissivity spectra are derived through a refinement process
281 based on LDA and these are used to estimate clear-sky simulated TB (TB_{sim}) using the ECMWF-AUX
282 atmospheric temperature and water vapor profiles. Then, the differences between the ~~TB_{sim} clear-sky simulated~~
283 TB and the ATMS observed TB (TB_{obs}) are evaluated ($\Delta TB_{obs-sim} = TB_{obs} - TB_{sim}$). Four ANNs are then applied to
284 a predictor set consisting of ATMS TB_{obs} , $\Delta TB_{obs-sim}$, a surface classification flag, and other ancillary parameters
285 (elevation and ATMS viewing angle for the final version). Finally, the pixels classified with the presence of
286 snowfall by the detection module, are used in the estimation modules while for no-snowfall flagged pixels the
287 snowfall rate value is set to 0 mm h^{-1} . In the following sections, the main blocks of the algorithm are described
288 in detail.

289 3.1 Surface Classification and ~~emissivity spectra estimation~~ Emissivity Spectra Estimation

290 3.1.1 PESCA Design and Performances

291 The dynamic classification and radiometric characterization of the background surface at the time of the satellite
292 overpass is based on PESCA exploiting ATMS low-frequency channels (Camplani et al, 2021). The algorithm
293 discriminates between frozen and unfrozen surfaces (sea ice and open water, snow-covered land and snow-free
294 land), and identifies 10 surface classes (4 over ocean, 5 over land, 1 for coast). The algorithm has been tuned
295 against the NOAA AutoSnow product (see Romanov, 2019), which gives daily maps of sea ice and snow cover.
296 For each ATMS observation, a flag reporting the AutoSnow class percentage (sea ice, open water, snow-covered
297 land, snow-free land) has been calculated; then, a threshold has been applied to discriminate between sea ice and
298 open water pixels (sea ice AutoSnow class $> 10 \%$) and between snow-covered and snow-free land pixels (snow-
299 covered land AutoSnow class $> 50 \%$). ATMS pixels have been classified into land, ocean, and coast pixels using
300 a land-sea mask.

301 The land module discriminates between snow-free land and snow-covered land and identifies four different snow
302 cover classes (Perennial, Winter Polar, Thin, and Deep Dry). It is based on a decision tree that makes use of a
303 limited number of inputs: the ratio between TB_{23QV} and TB_{31QV} (ratio), the difference between TB_{23QV} and
304 TB_{88QV} or Scattering Index (SI), 23 GHz pseudo-emissivity (pem_{23}) (i.e., the ratio between the 23 GHz
305 observed brightness temperature (TB) and the near-surface temperature value) (pem_{23}). The module has been
306 described by Camplani et al, 2021.

307 For what concerns the ocean module, a simple relationship to distinguish between sea ice and open water
 308 observations has been identified. In Figure 2 a Cartesian plane where the x-axis represents 23 GHz observed TBs
 309 and the y-axis represents the ~~near surface temperature~~ (T_{2m}) is shown. In the figure, each point represents a
 310 pseudo-emissivity value, and the color describes the mean AutoSnow sea ice percentage within each bin (see
 311 Figure 2, left panel). It is possible to observe that open water (0 % of sea ice, blue) and sea ice (100 % of sea ice,
 312 red) are characterized by very different pseudo-emissivities. There is a transition area between open water and sea
 313 ice pseudo-emissivity values for IFOVs where both open water and sea ice are present. The simple relationship
 314 for sea ice identification is reported in the left panel as a green line where the condition for sea ice identification
 315 is defined by Equation 1.

$$316 \quad TB_{23QV} > T_{2m} - 96 \text{ K}$$

317 (1)

318 Downstream of the sea ice/open water identification, information about sea ice characteristics is obtained from
 319 the analysis of the two low-frequency pseudo-emissivity ~~values~~ (pem_{23} and pem_{31}), ~~(defined as the ratio between~~
 320 ~~the observed TB and the near-surface temperature value)~~ which ~~are~~ can be considered a good approximation of
 321 sea-ice emissivity for low-frequency channels especially in cold and dry conditions. In Figure 3 (top panel) it is
 322 possible to observe that there are sea ice-classified observations characterized by the contemporary presence of
 323 open water and sea ice above the bisector of the plane and in correspondence with low emissivity values. In the
 324 center panel, where the color represents sea ice occurrences, it is evident the presence of one cluster, in
 325 correspondence with high pseudo-emissivity, with two “tails” above and below the bisector. This behavior has
 326 been used to identify 3 different sea ice classes (New Sea Ice, Broken Sea Ice, and Multilayer Sea Ice) using a
 327 Nearest Neighbor Method based on a set of reference points that define the areas of interest for each sea ice class.
 328 In Figure 3 (bottom panel) a classification representation is reported, where the markers represent the reference
 329 points. The labels of the classes have been chosen by analyzing their physical properties and by comparing the
 330 estimated emissivity spectra with those reported in previous studies (*Hewison & English, 1999, Munchak et al,*
 331 *2020*).

332 PESCA’s upper working limits for T_{2m} and TPW have been established to 280 K and 10 mm, respectively (see
 333 *Camplani et al, 2021* for details). Moreover, the land module does not work in the high elevation areas outside
 334 the polar regions (surface elevation > 2500 m for latitude < 67 ° N/S) because the ATMS low spatial resolution
 335 does not allow for depicting the small-scale snow-cover variability that characterizes the orographic regions. An
 336 analysis carried out using the ATMS-CPR coincidence dataset highlights that the presence of cloud cover does
 337 not influence the overall PESCA performances (not shown). Within these well-defined limits, ~~the~~ PESCA
 338 manages to optimally discriminate between sea ice, open water, snow-free land, and snow-covered land. The
 339 statistical scores of PESCA identification of sea ice and snow cover (using AutoSnow as ~~the~~ reference truth) are
 340 summarized in Table 1. In particular, the Probability of Detection (POD), the False Alarm Ratio (FAR), and the
 341 Heidke Skill Score (HSS) are reported. POD, FAR, and HSS are defined by equations 2, 3, and 4.

$$342 \quad POD = \frac{h}{h+m}$$

343 (2)

$$344 \quad FAR = \frac{f}{f+h}$$

345 (3)

$$346 \quad HSS = \frac{2(h*cn - f*m)}{(h+m)*(m+cn) + (h+f)*(f+cn)}$$

347 (4)

348 where h represents the hits, f represents the false alarms, m represents the misses and cn represents the correct
 349 negatives. PESCA manages to optimally detect the presence of a frozen background (sea ice over the ocean, snow
 350 covered land over the continental part) at the time of the satellite overpass. It is important to underline that the
 351 variability of the HSS compared to POD and FAR is due to the different number of correct negatives. An analysis
 352 of the physical characteristics of the PESCA classes has been conducted by considering the mean T_{2m} , ~~and~~ the
 353 geographical and seasonal distribution associated with each class. For what concerns the land classes, please refer
 354 to *Camplani et al, 2021*. For what concerns sea ice, the New Sea Ice class, which is detected during the winter at
 355 high latitudes and for low temperatures, represents the sea ice that forms during the winter. The Broken Sea Ice
 356 class, which is predominant in the lower latitudes and whose occurrence increases during the Spring season,
 357 represents the co-presence of sea ice and water. The Multilayer Sea Ice class, which is detected only at the high

latitudes, for very low temperatures, and constantly throughout the year, represents the ice pack typical of those regions and extreme cold conditions.

In Table 2 the number of PESCA class occurrences, the percentage of snowfall observations, and the most significant environmental characteristics in the ATMS-CPR coincident dataset are reported. It can be observed that Land and Ocean classes are characterized by the warmest/moistest conditions and by the most intense snowfall events (on average), while Perennial and Winter Polar Snow classes and New and Multilayer Sea Ice classes are characterized by the coldest/driest environmental conditions and by the lightest snowfall events (on average). Thin Snow and Broken Sea Ice classes show intermediate environmental conditions and snowfall intensity values. It is also interesting to highlight that a mismatch between the percentage of SWP and SSR observations is observed mostly over the Ocean class and, less frequently over other classes (Land, Thin Snow, and Coast), where warmer and moister environmental conditions are found.

3.1.2 PESCA emissivity spectra estimation

The emissivity spectra of each class have been estimated by applying the PESCA algorithm to the cloud-free (0% CPR cloud mask fraction) ATMS observations in the ATMS-CPR dataset satisfying PESCA working limits. The ATMS clear-sky TBs measured for each PESCA surface class have been used as input to an inverse radiative transfer model (RTM) based on plane-parallel approximation (Ulaby & Long, 2014) and the Rosenkrantz (1998) gas absorption model. The emissivity spectra have been estimated by calculating the mean and the standard deviation of the emissivity values for each class (excluding the values lower than the 10th percentile and higher than the 90th percentile). The emissivity spectra dependence on the ATMS viewing angle for polarized surfaces has been neglected because an analysis of such dependence in the ATMS-CPR coincidence dataset has shown that it is not significant (emissivity difference smaller than 0.05 for angles up to 52.7 °). This is due to the fact that cross-track scanning radiometers measure a signal (off-nadir) which derives from a mixture between the two polarizations (e.g., quasi-vertical, QV, and quasi-horizontal, QH). As a consequence, although the emissivities of polarized surfaces, such as open water surfaces, are strongly influenced by the viewing angle, the emissivity variation is compensated by the effect of the mixture of the two polarizations (see also Felde & Pickle, 1995, Prigent et al, 2000, Mathew et al, 2008, Prigent et al, 2017).

The estimated spectra are shown in Figure 4 and Figure 5 for ocean and land classes respectively (the coast has also been considered as a separate class; however, its spectrum is not shown in Figures 4-5). It is possible to observe that the classes are well-characterized from a radiometric point of view, showing distinct behavior of the emissivity spectra (e.g., the mean values). However, all the classes present significant standard deviations at high frequency, and some classes - such as the snow classes and the Broken Sea Ice class - present a high value of standard deviation also at low frequency.

The clear-sky RTM simulations based on the mean emissivity values estimated for each class have been compared to the coincident observed clear-sky TBs - but the RMSE between simulated and observed clear-sky TBs appeared to be too high to implement a robust signal analysis (>10 K). For this reason, a refinement process for the emissivity spectra estimation based on machine learning techniques has been developed downstream of the PESCA classification.

The refinement process has been based on a combination of an unsupervised classification technique (SOM) and a supervised technique (LDA). The unsupervised classification identifies clusters characterized by the minimum inner variability from a radiometric point of view. The supervised technique, instead, has the goal to identify the previously obtained clusters, and the associated emissivity spectra, by using only input variables that are not affected by the presence of clouds. The final emissivity spectra are estimated as the mean emissivity for each frequency within each cluster identified by the supervised technique. Therefore, as first step, the emissivity spectra have been clustered in order to minimize the emissivity variability in each cluster by arranging the retrieved emissivity values for six ATMS channels (23.8 GHz, 31.4 GHz, 50.3 GHz, 88.2 GHz, 165.5 GHz, and 183.31±7 GHz) in a one-dimensional SOM architecture. Then, an LDA model has been trained using the previously obtained clusters as reference and using the PESCA input parameters (pem_{23} , pem_{31} , $ratio$, and SI), some environmental parameters (TPW , T_{2m} , surface pressure - P_{surf}), and ancillary variables (latitude - lat , Julian day - jd , altitude - DEM , the maximum solar height during the day - H_{sun}) as input. The use of the LDA is necessary to associate an emissivity spectrum to all the observations which are classified by PESCA, independently of the presence of clouds. It is worth noticing that the whole predictor set of the LDA has resulted to be redundant; therefore, a subset of the predictors has been selected for each class. The accuracy of the LDA

410 classification is given by the ratio between the number of hits (observations where LDA identifies the associated
411 SOM class) and the total number of observations; it can be considered as an indicator of the effectiveness of the
412 LDA model in rebuilding the SOM results.

413 The evaluation of the refinement process is based on the comparison between the simulated clear-sky TBs
414 and the observed clear-sky TBs for each PESCA surface class. For each PESCA surface class, the number of
415 clusters that simultaneously lowers the errors (RMSE) between the simulated and observed clear-sky TBs at high
416 frequency (without lowering the classification accuracy too much) is chosen.

417 In Table 23 the number of clusters, the predictors selected, the accuracy, RMSE and percentage normalized root
418 mean squared error (NRMSE%) (Gareth et al, 2013) estimated on the test dataset, are reported for the 165.5 GHz
419 channel. NRMSE% is defined by Equation 5.

$$420 \quad NRMSE\% = \left(\frac{RMSE}{\sigma}\right) * 100$$

421 (5)

422 where σ represents the standard deviation of the measured clear-sky TBs dataset in each PESCA class. It can be
423 considered an indicator of the effectiveness of the refinement process.

424 For some classes, such as the Ocean class, the refinement process leads to low RMSE values (< 4 K). For other
425 classes, such as Deep Dry Snow and Broken Sea Ice, RMSE remains > 5 K even with a high number of clusters,
426 although there is a significant reduction compared to the initial variance in each class (NRMSE% < 50). This is
427 due to the variability of snow-covered background within each class; in the worst scenario, the limited number of
428 predictors are insufficient to infer the emissivity spectrum at high frequency. Overall, the refinement process
429 allows to obtain a general improvement of the accuracy of the dynamic emissivity estimation for the PESCA
430 classes; however, for some classes, the high-frequency channel uncertainty remains significant. The emissivity
431 spectra obtained by PESCA refinement are used as inputs of the RTM to obtain clear-sky simulated TBs (TB_{sim})
432 to be compared to the actual observations (TB_{obs}). The comparison between TB_{sim} clear-sky simulated TBs with
433 TB_{obs} observed TBs allows to highlight and interpret the MW signal in presence of snowfall.

434 In Figure 6, the snowfall signal is represented as a function of the SWP for the 165.5 GHz channel and for different
435 PESCA classes. The red line and shaded areas represent the mean values and standard deviations of the difference
436 between TB_{obs} and TB_{sim} observed TBs and clear-sky simulated TBs ($\Delta TB_{obs-sim} = TB_{obs} - TB_{sim}$) for SWP bins
437 calculated for observations where 2CSP SWP > 0 kg m⁻². The blue lines represent the uncertainty due to surface
438 emissivity variability for each PESCA class. They are centered on the estimated bias for each class (close to 0 K)
439 and the dashed lines correspond to the standard deviation of $\Delta TB_{obs-sim}$ in clear sky conditions. A clear scattering
440 signal ($\Delta TB_{obs-sim} < 0$) is observed over all the classes considered for intense snowfall events (SWP > 1 kg m⁻²).
441 For lower SWP values, the signal is more ambiguous and changes with the background surface. While over Land
442 there is a clear scattering signal for SWP > 0.1 kg m⁻², over the Perennial Snow class a scattering signal can be
443 observed only for SWP > 0.5 kg m⁻². For SWP < 0.1 kg m⁻², the mean $\Delta TB_{obs-sim}$ for snowfall observations is
444 less than its standard deviation in clear sky. This is due mainly to the emissivity variability for each surface class,
445 and to the error introduced by the use of model-derived temperature and water vapor profiles in the RT
446 simulations. However, while for the Land class the mean $\Delta TB_{obs-sim} < 0$ K can be explained as a predominant
447 scattering effect for all SWP values, for the Perennial Snow class the mean $\Delta TB_{obs-sim} > 0$ K can be interpreted as
448 a predominant emission signal with respect to the radiatively cold background (see Figure 5). The Thin Snow
449 class shows an intermediate behavior: for SWP < 0.1 kg m⁻² the red shaded area within the RMSE limits (blue
450 lines) of the RT simulations denotes the difficulty in interpreting the signal, while a clear scattering signal can be
451 observed for SWP > 0.3 kg m⁻². For what concerns ocean and new sea ice classes, a clear scattering signal is
452 visible only for high SWP values (> 1 kg m⁻²) while for low SWP values a significant emission signal is observed.
453 It is very likely that the emission effect observed over ocean and sea ice is likely generated by supercooled
454 cloud liquid water. The ubiquitous presence of supercooled water layers in snowing clouds (see Wang et al, 2013,
455 Battaglia & Panegrossi, 2020), especially over oceans (see Battaglia & Delanoë, 2013), generates an
456 emission effect which is particularly significant over radiatively cold surfaces (such as Perennial Snow, Ocean
457 and New Sea Ice at high frequency, see Figure 4), and can mask or overcome the weak scattering signal generated
458 by falling snow especially in light snowfall events. It is also important to underline that the DARDAR product
459 identifies mostly supercooled water layers at the cloud top (Rysman et al, 2018, Panegrossi et al, 2017), while it
460 has been shown that the impact of supercooled water layers embedded in the clouds can be very significant on the
461 measured TBs at MW high-frequency window channels (Battaglia & Panegrossi, 2020, Panegrossi et al, 2022).

3.2 ANN Design for ~~snowfall retrieval~~ Snowfall Retrieval

The snowfall detection and estimation modules have been based on ANNs. Four ANNs have been developed: two for the detection of SWP and SSR and two for the SWP and SSR estimate. The ~~performance~~ performances of more than 50 architectures have been tested, by varying the number of layers, the number of neurons for each layer, and the activation functions. The final architecture, for all modules, is composed of four layers: an input layer with a ~~neurons~~neuron number equal to the predictor number, ~~and~~ a hyperbolic tangent function as the activation function, a first hidden layer (60 neurons), and ~~a~~ hyperbolic tangent function, a second hidden layer (30 neurons), with a sigmoid function (for more information about the Neural Network characteristics, see *Sanò et al, 2015*). At the same time, several predictor sets have been tested combining in different ways ATMS $T_{B_{obs}}$, $\Delta T_{B_{obs-sim}}$, PESCA surface class, ATMS angle of view, ancillary information (surface elevation from a Digital Elevation Model), and model-derived environmental variables (T_{2m} , TPW, and ~~freezing level height~~the Freezing Level Height). In Table 34 the statistical scores of the algorithm performance for the SSR detection module obtained for different predictor sets are reported. It is possible to see that the best performance is obtained when the predictor set is composed of ATMS $T_{B_{obs}}$ and $\Delta T_{B_{obs-sim}}$, (besides ~~the~~ PESCA surface flag, the pixel ~~surface~~ elevation, and the cosine of the viewing angle). In particular, it is notable the improvement of the detection capabilities with respect to a predictor set composed of ATMS $T_{B_{obs}}$ and environmental parameters, ~~which is used in other approaches such as that of SLALOM-CT~~. On the other hand, the simultaneous use of both the $\Delta T_{B_{obs-sim}}$ and the environmental parameters show scores almost equal to that obtained by using only $\Delta T_{B_{obs-sim}}$. This indicates that the computation of the multi-channel clear-sky TBs at the time of the overpass through the estimation of the dynamic surface class emissivity spectra and its deviation from the measured TBs plays a fundamental role in snowfall retrieval, ~~in particular in cold/dry environmental conditions~~. It provides essential information to the ANN to be able to exploit the subtle snowfall-related signal in ATMS measurements. This is the most innovative aspect of HANDEL-ATMS.

Based on these results, the final set of predictors for HANDEL-ATMS is composed ~~by 16 ATMS~~of 16 ATMS channels $T_{B_{obs}}$ (1-9, 16-22, channels 10-15 have not been considered because their weighting function peaks above the tropopause), and the corresponding $\Delta T_{B_{obs-sim}}$, the PESCA classification flag, the pixel elevation (obtained from a DEM) and the cosine of the ~~view~~viewing angle.

4. Results

4.1 HANDEL-ATMS Performances

In Table 4-5 the statistical scores of HANDEL-ATMS detection module performances are reported in terms of POD, FAR ~~and HSS~~. ~~It is possible to observe good detection capabilities both for SWP and SSR modules (POD > 0.8, FAR < 0.2), and HSS. These statistical scores - and the plot reported in the next figures - have been calculated for the test dataset.~~

In Figure 7 and ~~in~~Figure 8 the dependence of HANDEL-ATMS snowfall detection statistical scores on TPW and ~~on~~ T_{2m} is reported. In both figures, it is possible to observe that the SWP detection capabilities improve (with an increase of POD and HSS and a decrease of FAR) with increasing humidity and temperature. This is due to the combined effect of a stronger scattering signal associated with more intense snowfall events - linked to moister and warmer environmental conditions, ~~as can be observed in Figure 12 and Table 2~~ - and to the lower transmissivity of the atmosphere which masks the background surface signal, reducing its impact and the uncertainties linked to its variability. On the other hand, colder and drier conditions are usually linked to background surface types characterized by high radiometric variability such as Perennial Snow and Winter Polar Snow classes, which cause uncertainty in emissivity estimation. It is possible to observe that in Figure 7 SSR detection capabilities show a maximum HSS value for TPW between 3 mm and 5 mm, and then there is a slight decrease due to the decrease of POD. A similar situation can be observed in Figure 8, where ~~the~~ HSS reaches a maximum between 250 K and 275 K, and it is lower than for SWP. This is due to the fact that PMW measurements respond mostly to the snow in the atmospheric column and in moister/warmer conditions the presence of snow in the atmosphere is not always linked to surface snowfall. In both cases, it is worth noting that also considering very dry (TPW \approx 2 mm) or very cold ($T_{2m} \approx$ 240 K) conditions, HANDEL-ATMS shows good detection capabilities, in spite of the uncertainties linked to the modeling of the background surface and the weakness of the signal in such conditions. ~~Moreover,~~In Figure 9 the dependence of HANDEL-ATMS snowfall detection statistical scores on SWP and SSR values retrieved by CPR 2CSP is reported. Only POD is reported because the statistics are calculated for snowfall observations only (2CSP SWP/SSR > 0 kg m⁻²/mm h⁻¹). It is possible to observe that also

514 considering very low SWP and SSR values ($SWP \approx 0.001 \text{ kg m}^{-2}$, $SSR \approx 0.001 \text{ mm h}^{-1}$), HANDEL-ATMS
515 manages to detect around 60 % of the snowfall events. ~~Similar considerations can be done also for the different~~
516 ~~background surfaces.~~

517 The detection capabilities are influenced both by the typical environmental conditions of each PESCA class and
518 by the uncertainties linked to the emissivity estimation. In Figure 910 the statistical scores of the algorithm
519 performance by considering each PESCA class for both the SWP and the SSR detection module are reported. It
520 can be observed that, also considering specifically the classes associated ~~to~~with extremely dry and cold
521 environmental conditions such as Perennial Snow or Winter Polar Snow (see *Camplani et al, 2021 and Table 2*),
522 where the detection is more problematic due to ~~the~~low snowfall intensity (see Table 2) and to the uncertainties in
523 the emissivity retrieval (see Table 2), ~~and to the low snowfall intensity,~~ 3), HANDEL-ATMS has good detection
524 capabilities (POD and FAR values greater than 0.7 and less than 0.25, respectively, for both SWP and SSR). On
525 the other hand, for surface classes characterized by the highest emission estimation uncertainties, such as Deep
526 Dry Snow, the statistical scores are coherent with the general scores and better than those obtained in presence of
527 extremely dry/cold environmental conditions. So, it is possible to conclude that the extremely cold/dry
528 environmental conditions ~~—~~have more influence on the detection than the uncertainties on clear sky emissivity
529 estimation. ~~—~~ Generally, these results provide evidence that HANDEL-ATMS can be used to analyze snowfall
530 occurrence in the polar regions.

531 The error statistics of the two estimation modules are reported in Table 56 in terms of bias, RMSE and the
532 coefficient of determination R^2 , which is defined by Equation 6.

$$R^2 = 1 - \frac{RMSE^2}{std^2}$$

533
534 (6)

535 It is worth noticing that the biases are negligible for both modules while RMSE values are comparable to the light
536 events recorded in the dataset. Moreover, as expected, RMSE and R^2 values are respectively higher and lower for
537 the SSR module than for the SWP module. In Figure 1011 the density scatterplots between the SWP and SSR
538 values retrieved by HANDEL-ATMS and ~~the~~2CSP corresponding values are reported. For both modules, an
539 overestimation can be observed for very light snowfall ($SWP < 10^{-2} \text{ kg m}^{-2}$ and $SSR < 10^{-2} \text{ mm h}^{-1}$), while there
540 is a very good agreement for higher SWP and SSR values. In order to relate these results to the environmental
541 conditions, Figure 1112 shows the dependence of HANDEL-ATMS snowfall estimation error statistics, as well
542 ~~of~~as SWP and SSR, on TPW. The curves represent, for each 1-mm TPW bin, the mean ~~2-CSP~~2CSP SWP or SSR
543 computed, the RMSE, and the relative bias (the ratio between the bias and the SWP/SSR mean value for each
544 bin). As expected, TPW and snowfall intensity are strongly correlated. An increase ~~of~~in the absolute RMSE can
545 be observed as TPW increases, and it is larger than the SWP/SSR mean value for $TPW < 8 \text{ mm}$. A similar behavior
546 can be observed by analyzing the dependence of HANDEL-ATMS snowfall estimation error statistics on T_{2m} (not
547 shown). A very moderate overestimation is observed for $TPW < 8 \text{ mm}$ and for lower SWP and SSR values ($<$
548 0.1 mm h^{-1}), with relative bias around 5%, (up to 8% only for extremely low TPW values and very low number
549 of observations ~~(, see Figure 7))~~), while underestimation (relative bias up to -5%) is observed for higher TPW
550 values and higher SWP and SSR values. Generally, light snowfall events are linked to the very cold/dry
551 environmental conditions typical of high-latitude regions. So, the algorithm manages to estimate also the very
552 light SWP and SSR typical of high latitudes but tends to slightly overestimate snowfall intensity in such
553 conditions.

554 From the analysis of Figure 7-1112, it can be concluded that HANDEL-ATMS has good detection capabilities
555 (also for extremely light snowfall) but it shows some limitations in correctly estimating its intensity, with slight
556 overestimation of the very light snowfall typical of high latitudes.

557 4.2 A Case Study: Greenland-2016/04/24

558 The case study reported corresponds to the observation of a moderately light snowfall event over the central part
559 of Greenland that occurred on 24 April 2016. ATMS overpass is between 14:51:23 UTC. and 14:57:47 UTC.,
560 while the CPR overpass is between 15:05:25 UTC. and 15:11:45 UTC., with a time difference of 14 minutes and
561 2 seconds. This event presents several characteristics typical of high latitudes, such as light snowfall rate, dry and
562 cold atmospheric conditions, and presence of a frozen background surface, a typical case of interest for the
563 application of HANDEL-ATMS.
564

565 In Figure 4213 PESCA classification is reported. The entire territory of Greenland, except for a narrow area on
566 the southwestern coast, is identified as a snow-covered surface; the PESCA identifies the Perennial Snow class in
567 the central part of Greenland and along the CloudSat track, and the Polar Winter Snow class near the northern
568 shoreline. CloudSat overpasses the central part of the island, and the CPR track is along the central part of the
569 ATMS swath.

570 In Figure 4314 a synopsis of the event along the CPR track is reported showing T_{2m} and TPW, the 2CSP SWP
571 and SSR values, and the cross-section of CPR reflectivity, with the DARDAR supercooled water information
572 superimposed (in magenta). Moreover, the PESCA surface classification, and the TBs of the main ATMS high-
573 frequency channels along the CloudSat track are also shown. The event is characterized by dry conditions (TPW
574 < 5 mm) and T_{2m} below 273 K, except over the coast. CPR observes a cloud system associated with the snowfall
575 event between 68°N and 76°N ; DARDAR detects the presence of a supercooled water layer at the cloud top
576 between 68°N and 72°N and indicates the presence of supercooled droplets embedded in the deeper cloud
577 associated with the more intense snowfall. According to the 2CSP product, a light shallow snowfall system is
578 found in the inner part of the island while deeper, more intense snowfall, with a peak of intensity between 72°N
579 and 76°N , is found near the shoreline. For what concerns the associated ATMS observations, an increase of
580 the 88 GHz and 165 GHz TBs is observed in correspondence with the supercooled water layer, while only a slight
581 decrease of 165.5 and 183.3 ± 7 GHz TBs can be observed in coincidence with the snowfall intensity peak.

582 In Figure 12Figure 15 the maps of the TB_{obs} at 165.5 GHz (top panel) and the $\Delta TB_{obs-sim}$ at 165.5 GHz (bottom
583 panel) are reported. In the top panel, it is possible to observe that, despite the snowfall event, there is not a clear
584 TB scattering signal in the area where 2CSP detects snowfall ($70^{\circ}\text{N} - 76^{\circ}\text{N}$, $40^{\circ}\text{W} - 70^{\circ}\text{W}$), instead a
585 slight increase in the TBs can be observed in the area where DARDAR detects the supercooled water layer at the
586 cloud top. The map of $\Delta TB_{obs-sim}$ allows to observe shows an emission signal ($\Delta TB_{obs-sim} > 0$) over the central part
587 of the ATMS swath due to the combined effect of the emission by the supercooled liquid water layers at the cloud
588 top, as evidenced by DARDAR, (evidently exceeding the scattering signal of the weak and shallow snowfall),
589 over a radiatively cold surface background. Only near the shoreline, the TB_{obs} observed TBs are slightly lower
590 than the TB_{sim} clear-sky simulated TBs ($\Delta TB_{obs-sim} < 0$) due to the stronger scattering signal of the deeper snowfall
591 system. In Figure 1516 the results of the HANDEL-ATMS four modules are reported. It is worth noting that both
592 detection modules find snowfall in the central region of Greenland and near the northern coast. The estimated
593 snowfall intensity for this event is generally low (SWP < 0.1 kg m^{-2} and SSR < 0.1 mm h^{-1}) except over the
594 western coast, where SWP reaches 0.5 kg m^{-2} and SSR reaches 1 mm h^{-1} . It is worth noticing that HANDEL-
595 ATMS detects snowfall also where there is an emission signal ($\Delta TB_{obs-sim} > 0$) and that discontinuities in snowfall
596 retrievals are not observed in correspondence with surface class changes.

597 Finally, a comparison between the HANDEL-ATMS and the 2CSP is reported in Figure 1617. There is a
598 substantial agreement on the snowfall detection of the two products. It can be observed that HANDEL-ATMS
599 tends to overestimate very light SWP and SSR in presence of the shallow system (2CSP SWP < 0.05 kg m^{-2} and
600 SSR < 0.1 mm h^{-1} , between 68°N and 72°N), consistently with what is shown in Figure 10, while there is a
601 good agreement between 72°N and 76°N , where snowfall intensity increases.

602 The analysis of this case study demonstrates that the algorithm can interpret the ambiguity of the
603 emission/scattering signal often associated with snowfall events at high latitudes (as described in Section 4.1) and
604 efficiently detect, and, to a less extent, quantify snowfall even in extreme cold and dry conditions.

605 4.3 Comparison with SLALOM-CT

606 SLALOM-CT has been introduced in Section 1. It presents some similarities with HANDEL-ATMS: it is based
607 on an ANN approach and uses the CPR-2CSP product as reference. On the other hand, substantial differences
608 have to be highlighted: SLALOM-CT was designed to operate on a global scale, while HANDEL-ATMS has been
609 developed specifically for the environmental conditions typical of high latitudes. Moreover, the predictor sets are
610 different: in addition to TB observations, SLALOM-CT relies on several model-derived environmental
611 parameters, while HANDEL-ATMS relies on differences between simulated clear-sky TBs, based on the dynamic
612 estimation of the background surface emissivity (i.e., at the time of the satellite overpass), and observed TBs
613 ($\Delta TB_{obs-sim}$), as described in Section 3.

614 In Table 67 a comparison between the statistical scores of the detection performances of the two algorithms is
615 reported for different environmental conditions. The comparison has been carried out considering the same
616 elements of the ATMS-CPR coincidence dataset. It can be observed that the differences between the two algorithm

performances increase as the environmental conditions become more extreme (i.e., lower T_{2m} and TPW), with consistently better snowfall detection capabilities of HANDEL-ATMS than SLALOM-CT. Considering the working limits of HANDEL-ATMS, POD increases by 2 % and FAR decreases by 8 %, while for very cold/dry conditions ($T_{2m} < 250$ K, TPW < 5 mm), POD increases by 7 % and FAR decreases by 16 %; for extremely dry/cold conditions ($T_{2m} < 240$ K, TPW < 3 mm), typical of the inner part of Greenland and Antarctica, POD increases by 18 % and FAR decreases by 16 %.

5 Conclusions and Future Perspectives

In this paper, a new snowfall retrieval algorithm, the High Latitude sNow Detection and Estimation aLgorithm for ATMS (HANDEL-ATMS), is described. The algorithm is based on machine learning techniques trained with CPR 2CSP snowfall product and it is designed specifically for the cold and dry environmental conditions typical of high-latitude regions. The driving and innovative principle in the algorithm development is the exploitation of the full range of ATMS channel frequencies to characterize the background surface radiative properties at the time of the overpass to be able to better isolate and interpret the snowfall-related contribution to the measured multi-channel upwelling radiation. A similar approach has been used by *Zhao & Weng, 2002*; however, their application was limited to non-scattering surfaces and was based on empirical relationships. This approach is proven to be effective for snowfall detection and quantification at high latitudes, particularly in presence of a frozen (snow-covered land or sea ice) background surface, also compared to other state-of-the-art machine learning-based methods.

HANDEL-ATMS can detect snowfall at high latitudes in good agreement with CPR. The estimation modules tend to slightly overestimate the intensity of light snowfall events ($SWP < 10^{-2}$ kg m⁻²), with mean relative bias < 5% for $SSR < 0.1$ mm h⁻¹, but it shows good accuracy for more intense snowfall events ($SWP > 10^{-2}$ kg m⁻², $SWP < 1$ kg m⁻²). It is worth noting, however, that the uncertainty associated with the surface emissivity estimation in some conditions affects the capabilities of HANDEL-ATMS to correctly interpret the snowfall signature. Such uncertainty propagates in the RTM simulation of clear-sky TBs used as input in the algorithm. Despite these limitations, it is worth noticing that the development of an algorithm capable of retrieving snowfall at high latitudes with good accuracy is an important development in the climate science field. The possibility to exploit the high temporal sampling of the near-polar operational satellites carrying ATMS radiometers allows to achieve full coverage of the polar regions. Moreover, the future European MetOp Second Generation (MetOp-SG) mission, with the launch of the Sat-A Microwave Sounder (MWS), with characteristics very similar to ATMS, will soon provide additional coverage to improve global snowfall monitoring. The HANDEL-ATMS methodology will be adapted to be able to exploit MWS measurements in the future. The capability to estimate snowfall at high temporal resolution is ancillary to the development of a snowfall monitoring system for the high latitudes and to the analysis of the snowfall climatology in these areas, with possible applications in climate change studies in the polar regions.

Future research will address some open issues. The estimation of the surface emissivity and the simulated clear-sky multi-channel TBs needs to be further improved, either by considering other predictor sets or by using a different technique for the emissivity spectra definition including a more advanced RTM. Another important aspect is the quantification of the error linked to the background surface emissivity estimation on the snowfall detection capabilities. This would be also useful for the development of modules for mountainous areas, which have not been considered in the current version of the algorithm. Moreover, the effect on the algorithm snowfall detection capabilities of the uncertainties linked to the model-derived environmental variables (e.g., temperature and water vapor profile), which are used in the clear-sky TB simulations, should be investigated. The use of the ATMS water vapor (183 GHz band) and temperature (50 GHz band) sounding channels to characterize the atmospheric conditions at the time of the overpass in order to complement or avoid the use of model-derived data is another subject of future research. Moreover, the development of a separate supercooled liquid water detection module will be also evaluated, similarly to what is done in other PMW snowfall detection and estimation algorithms (*Rysman et al, 2018, Sanò et al, 2022*). Such information can be exploited to improve snowfall detection and estimation capabilities since the emission by the cloud droplets in dry conditions tends to mask the snowfall scattering signal (*see Panegrossi et al, 2017, Panegrossi et al, 2022*), and adds larger uncertainties in the CPR snowfall products used as reference (*Battaglia & Panegrossi, 2021*). Moreover, recent studies have highlighted that TBs correlate more strongly with lagged surface precipitation (with a time lag of 30-60 min for snowfall) than the simultaneous precipitation rate (*see You et al, 2019*). Therefore, an analysis based on a

669 coincident dataset characterized by different time lags will be conducted. The results of this analysis will be
670 compared with HANDEL-ATMS performances in order to identify a way to exploit this information towards the
671 improvement of SSR detection and estimation. Finally, since the algorithm has been developed only for specific
672 environmental conditions typical mostly of high latitudes an integration with other approaches, such as [that of the](#)
673 SLALOM-CT, designed for global estimation of snowfall, could be considered in the future to improve global
674 snowfall monitoring based on ATMS and on future cross-track scanning radiometers.

675 **Data ~~availability~~Availability**

676 ATMS data are provided by the NOAA CLASS facility www.avl.class.noaa.gov/ (last access 4 ~~april~~April 2023),
677 CPR data are distributed by the CloudSat data processing center <https://www.cloudsat.cira.colostate.edu/> (last
678 access 4 ~~april~~April 2023), DARDAR data are available from the ICARE FTP server of the University of Lille
679 (<ftp.icare.univ-lille1.fr>, last access 4 ~~april~~April 2023) and ECMWF operational forecasts are distributed by
680 ECMWF through the MARS facility via the ECGATE cluster. AutoSnow data are provided by -the NOAA
681 Satellite and Information Service https://satepsanone.nesdis.noaa.gov/northern_hemisphere_multisensor.html
682 (last access 4 ~~april~~April 2023).

683 **Author Contribution**

684 Conceptualization, A.C., P.S., D.C.; methodology, A.C., P.S., D.C.; software, A.C.; validation, A.C.; formal
685 analysis, A.C.; investigation, A.C., P.S., D.C., G.P.; data curation, A.C. and D.C.; writing—original draft
686 preparation, A.C.; writing—review and editing, A.C., P.S., D.C., and G.P.; visualization, A.C.; supervision, G.P.;
687 project administration, G.P.; funding acquisition, G.P. All authors have read and agreed to the published version
688 of the manuscript.

689 **Competing Interests**

690 The authors declare no conflict of interest. The funders had no role in the design of the study; in the collection,
691 analyses, or interpretation of data; in the writing of the manuscript, or in the decision to publish the results.

692 **Acknowledgements**

693 **Acknowledgments**

694 This work was carried out under the RainCast study (ESA Contract No. 4000125959/18/NL/NA) and by the
695 EUMETSAT Satellite Application Facility for Operational Hydrology and Water management (H SAF) Third and
696 Fourth Continuous and Operations Phase (CDOP-3 and CDOP-4). Andrea Camplani was supported by the Ph.D.
697 program in Infrastructures, Transport Systems, and Geomatics at the Department of Civil, Constructional, and
698 Environmental Engineering at Sapienza University of Rome. The authors would like to thank EUMETSAT and
699 the NASA Precipitation Measurement Mission (PMM) Research Program for supporting scientific collaborations
700 between H SAF and GPM, and the PMM Science Team. The authors wish to express their sincere gratitude to Joe
701 Turk (NASA JPL) and Alessandro Battaglia who are warmly acknowledged for useful interactions and discussions
702 during the algorithm development and validation, and to Mattia Crespi for the scientific support to Andrea
703 Camplani during the Ph.D. program.

704 **References**

- 705 Battaglia, A., & Delanoë, J.: Synergies and complementarities of CloudSat-CALIPSO snow observations. *Journal*
706 *of Geophysical Research: Atmospheres*, 118(2), 721-731. <https://doi.org/10.1029/2012JD018092>, 2013.
- 707 Battaglia, A., & Panegrossi, G.: What can we learn from the CloudSat radiometric mode observations of snowfall
708 over the ice-free ocean? *Remote Sensing*, 12(20), 3285, <https://doi.org/10.3390/rs12203285>, 2020.
- 709 Behrangi, A., Christensen, M., Richardson, M., Lebsack, M., Stephens, G., Huffman, G. J., Bolvin, D., Adler, R.
710 F., Gardner, A., Lambrightsten, B., & Fetzer, E.: Status of high-latitude precipitation estimates from observations
711 and reanalyses. *Journal of Geophysical Research: Atmospheres*, 121(9), 4468-4486,
712 <https://doi.org/10.1002/2015JD024546>, 2016.
- 713 Bintanja, R., Selten, F.: Future increases in Arctic precipitation linked to local evaporation and sea-ice retreat.
714 *Nature* 509, 479–482, <https://doi.org/10.1038/nature13259>, 2014.
- 715 Camplani, A., Casella, D., Sanò, P., & Panegrossi, G.: The Passive microwave Empirical cold Surface
716 Classification Algorithm (PESCA): Application to GMI and ATMS. *Journal of Hydrometeorology*, 22(7), 1727-
717 1744, <https://doi.org/10.1175/JHM-D-20-0260.1>, 2021.

719 Casella, D., Panegrossi, G., Sanò, P., Marra, A. C., Dietrich, S., Johnson, B. T., & Kulie, M. S.: Evaluation of the
720 GPM-DPR snowfall detection capability: Comparison with CloudSat-CPR. *Atmospheric Research*, 197, 64-75,
721 <https://doi.org/10.1016/j.atmosres.2017.06.018>, 2017.

722 Ceccaldi, M., Delanoë, J., Hogan, R. J., Pounder, N. L., Protat, A., & Pelon, J.: From CloudSat-CALIPSO to
723 EarthCare: Evolution of the DARDAR cloud classification and its comparison to airborne radar-lidar
724 observations. *Journal of Geophysical Research: Atmospheres*, 118(14), 7962-7981,
725 <https://doi.org/10.1002/jgrd.50579>, 2013.

726 DARDAR- retrieve cloud properties by combining the CloudSat radar and the CALIPSO lidar measurements.
727 CNS-CNRS-Université de Lille., <https://www.icare.univ-lille.fr/dardar/>, last access: 4 April 2023.

728 Clifford, D.: Global estimates of snow water equivalent from passive microwave instruments: history, challenges
729 and future developments. *International Journal of Remote Sensing*, 31(14), 3707-3726,
730 <https://doi.org/10.1080/01431161.2010.483482>, 2010.

731 Comiso, J. C.: Sea ice effective microwave emissivities from satellite passive microwave and infrared
732 observations. *Journal of Geophysical Research: Oceans*, 88(C12), 7686-7704.
733 <https://doi.org/10.1029/JC088iC12p07686>, 1983

734 Cordisco, E., Prigent, C., & Aires, F.: Snow characterization at a global scale with passive microwave satellite
735 observations. *Journal of Geophysical Research: Atmospheres*, 111(D19), <https://doi.org/10.1029/2005JD006773>,
736 2006.

737 [Delanoë, J., and R. J. Hogan: Combined CloudSat-CALIPSO-MODIS retrievals of the properties of ice clouds. *J.*](#)
738 [Geophys. Res.](#), 115, D00H29, doi:10.1029/2009JD012346, 2010.

739 Fausett, L. V., Fundamentals of neural networks: architectures, algorithms and applications, Pearson Education
740 India, ISBN-13: 978-0133341867, 1994.

741 Felde, G. W., & Pickle, J. D.: Retrieval of 91 and 150 GHz Earth surface emissivities. *Journal of Geophysical*
742 *Research: Atmospheres*, 100(D10), 20855-20866, <https://doi.org/10.1029/95JD02221>, 1995.

743 Gareth, J., Daniela, W., Trevor, H., & Robert, T.: An introduction to statistical learning: with applications in R.
744 Springer, ISBN-13:978-1461471370 , 2013.

745 Grody, N. C., & Basist, A. N.: Global identification of snowcover using SSM/I measurements. *IEEE Transactions*
746 *on geoscience and remote sensing*, 34(1), 237-249, DOI: 10.1109/36.481908, 1996.

747 Hastie, T., Tibshirani, R., Friedman, J. H., & Friedman, J. H.: *The elements of statistical learning: data mining,*
748 *inference, and prediction* (Vol. 2, pp. 1-758). New York: springer, DOI: 10.1007/b94608, 2009.

749 [Kidd, C., Becker, A., Huffman, G. J., Muller, C. L., Joe, P., Skofronick-Jackson, G., & Kirschbaum, D. B.: So,](#)
750 [how much of the Earth's surface is covered by rain gauges?. *Bulletin of the American Meteorological Society,*](#)
751 [98\(1\), 69-78, <https://doi.org/10.1175/BAMS-D-14-00283.1>, 2017.](#)

752 Kidd, C., & Huffman, G.: Global precipitation measurement. *Meteorological Applications*, 18(3), 334-353,
753 <https://doi.org/10.1002/met.284>, 2011.

754 Hewison, T. J., & English, S. J.: Airborne retrievals of snow and ice surface emissivity at millimeter wavelengths.
755 *IEEE Transactions on Geoscience and Remote Sensing*, 37(4), 1871-1879, DOI: 10.1109/36.774700, 1999.

756 Kim, M. J., Weinman, J. A., Olson, W. S., Chang, D. E., Skofronick-Jackson, G., & Wang, J. R.: A physical
757 model to estimate snowfall over land using AMSU-B observations. *Journal of Geophysical Research:*
758 *Atmospheres*, 113(D9), <https://doi.org/10.1029/2007JD008589>, 2008.

759 Kohonen, T.: *Self-organization and associative memory* (Vol. 8). Springer Science & Business Media,
760 DOI:10.1007/978-3-642-88163-3, 2012.

761 Kongoli, C., Pellegrino, P., Ferraro, R. R., Grody, N. C., & Meng, H.: A new snowfall detection algorithm over
762 land using measurements from the Advanced Microwave Sounding Unit (AMSU). *Geophysical Research Letters*,
763 30(14). <https://doi.org/10.1029/2003GL017177>, 2003.

764 Kongoli, C., Meng, H., Dong, J., & Ferraro, R.: A snowfall detection algorithm over land utilizing high-frequency
765 passive microwave measurements—Application to ATMS. *Journal of Geophysical Research: Atmospheres*,
766 120(5), 1918-1932, <https://doi.org/10.1002/2014JD022427>, 2015.

767 Kongoli, C., Meng, H., Dong, J., & Ferraro, R.: A hybrid snowfall detection method from satellite passive
768 microwave measurements and global forecast weather models. *Quarterly Journal of the Royal Meteorological*
769 *Society*, 144, 120-132. <https://doi.org/10.1002/qj.3270>, 2018.

770 Kulie, M. S., Bennartz, R., Greenwald, T. J., Chen, Y., & Weng, F.: Uncertainties in microwave properties of
771 frozen precipitation: Implications for remote sensing and data assimilation. *Journal of the Atmospheric Sciences*,
772 67(11), 3471-3487. <https://doi.org/10.1175/2010JAS3520.1>, 2010.

773 Kulie, M. S., Milani, L., Wood, N. B., Tushaus, S. A., Bennartz, R., & L'Ecuyer, T. S.: A shallow cumuliform
774 snowfall census using spaceborne radar. *Journal of Hydrometeorology*, 17(4), 1261-1279.
775 <https://doi.org/10.1175/JHM-D-15-0123.1>, 2016.

776 Levizzani, V., Laviola, S., & Cattani, E.: Detection and measurement of snowfall from space. *Remote Sensing*,
777 3(1), 145-166, <https://doi.org/10.3390/rs3010145>, 2011.

778 Liu, Y., Key, J. R., Liu, Z., Wang, X., & Vavrus, S. J.: A cloudier Arctic expected with diminishing sea ice.
779 *Geophysical Research Letters*, 39(5). <https://doi.org/10.1029/2012GL051251>, 2012.

780 Liu, J., Curry, J. A., Wang, H., Song, M., & Horton, R. M.: Impact of declining Arctic sea ice on winter snowfall.
781 *Proceedings of the National Academy of Sciences*, 109(11), 4074-4079. <https://doi.org/10.1073/pnas.1114910109>,
782 2012.

783 Liu, G., & Seo, E. K.: Detecting snowfall over land by satellite high-frequency microwave observations: The lack
784 of scattering signature and a statistical approach. *Journal of geophysical research: atmospheres*, 118(3), 1376-
785 1387, <https://doi.org/10.1002/jgrd.50172>, 2013.

786 Mathew, N., Heygster, G., Melsheimer, C., & Kaleschke, L.: Surface emissivity of Arctic sea ice at AMSU
787 window frequencies. *IEEE transactions on geoscience and remote sensing*, 46(8), 2298-2306,
788 DOI:10.1109/TGRS.2008.916630, 2008.

789 Mätzler, C., & Hüppi, R.: Review of signature studies for microwave remote sensing of snowpacks. *Advances in*
790 *Space Research*, 9(1), 253-265, [https://doi.org/10.1016/0273-1177\(89\)90493-6](https://doi.org/10.1016/0273-1177(89)90493-6), 1989.

791 Meng, H., Dong, J., Ferraro, R., Yan, B., Zhao, L., Kongoli, C., Wang, N., & Zavadsky, B.: A 1DVAR-based
792 snowfall rate retrieval algorithm for passive microwave radiometers. *Journal of Geophysical Research:*
793 *Atmospheres*, 122(12), 6520-6540. <https://doi.org/10.1002/2016JD026325>, 2017.

794 Milani, L., Kulie, M. S., Casella, D., Dietrich, S., L'Ecuyer, T. S., Panegrossi, G., Porcù, F., Sanò, P., & Wood,
795 N. B.: CloudSat snowfall estimates over Antarctica and the Southern Ocean: An assessment of independent
796 retrieval methodologies and multi-year snowfall analysis. *Atmospheric research*, 213, 121-135,
797 <https://doi.org/10.1016/j.atmosres.2018.05.015>, 2018.

798 Milani, L., & Wood, N. B.: Biases in cloudsat falling snow estimates resulting from daylight-only operations.
799 *Remote Sensing*, 13(11), 2041, <https://doi.org/10.3390/rs13112041>, 2021.

800 Mroz, K., Montopoli, M., Battaglia, A., Panegrossi, G., Kirstetter, P., & Baldini, L.: Cross validation of active
801 and passive microwave snowfall products over the continental United States. *Journal of Hydrometeorology*, 22(5),
802 1297-1315. <https://doi.org/10.1175/JHM-D-20-0222.1>, 2021.

803 Munchak, S. J., Ringerud, S., Brucker, L., You, Y., de Gelis, I., & Prigent, C.: An active-passive microwave land
804 surface database from GPM. *IEEE Transactions on Geoscience and Remote Sensing*, 58(9), 6224-6242, DOI:
805 10.1109/TGRS.2020.2975477, 2020.

806 Noh, Y. J., Liu, G., Jones, A. S., & Vonder Haar, T. H.: Toward snowfall retrieval over land by combining satellite
807 and in situ measurements. *Journal of Geophysical Research: Atmospheres*, 114(D24),
808 <https://doi.org/10.1029/2009JD012307>, 2009.

809 Panegrossi, G., Rysman, J. F., Casella, D., Marra, A. C., Sanò, P., & Kulie, M. S.: CloudSat-based assessment of
810 GPM Microwave Imager snowfall observation capabilities. *Remote Sensing*, 9(12), 1263,
811 <https://doi.org/10.3390/rs9121263>, 2017.

812 Panegrossi, G., Casella, D., Sanò, P., Camplani, A., & Battaglia, A.: Recent advances and challenges in satellite-
813 based snowfall detection and estimation. *Precipitation Science*, 333-376, <https://doi.org/10.1016/B978-0-12-822973-6.00015-9>, 2022.

815 Partain, P.: CloudSat ECMWF-AUX Auxiliary Data Product Process Description and Interface Control
816 Document, Product Version P1_R05, NASA JPL CloudSat project document revision 0, pp. 16, Available from:
817 [https://www.cloudsat.cira.colostate.edu/cloudsat-static/info/dl/ecmwf-aux/ECMWF-](https://www.cloudsat.cira.colostate.edu/cloudsat-static/info/dl/ecmwf-aux/ECMWF-AUX.PDICD.P1_R05.rev0.pdf)
818 [AUX.PDICD.P1_R05.rev0.pdf](https://www.cloudsat.cira.colostate.edu/cloudsat-static/info/dl/ecmwf-aux/ECMWF-AUX.PDICD.P1_R05.rev0.pdf), 2022

819 Prigent, C., Wigneron, J. P., Rossow, W. B., & Pardo-Carrion, J. R.: Frequency and angular variations of land
820 surface microwave emissivities: Can we estimate SSM/T and AMSU emissivities from SSM/I emissivities?. *IEEE*
821 *transactions on geoscience and remote sensing*, 38(5), 2373-2386, DOI:10.1109/36.868893, 2000.

822 Prigent, C., Aires, F., Rossow, W., & Matthews, E.: Joint characterization of vegetation by satellite observations
823 from visible to microwave wavelengths: A sensitivity analysis. *Journal of Geophysical Research: Atmospheres*,
824 *106*(D18), 20665-20685, <https://doi.org/10.1029/2000JD900801>, 2001.

825 Prigent, C., Jaumouille, E., Chevallier, F., & Aires, F.: A parameterization of the microwave land surface
826 emissivity between 19 and 100 GHz, anchored to satellite-derived estimates. *IEEE Transactions on Geoscience
827 and Remote Sensing*, *46*(2), 344-352, DOI: 10.1109/TGRS.2007.908881, 2008.

828 Prigent, C., Aires, F., Wang, D., Fox, S., & Harlow, C.: Sea-surface emissivity parametrization from microwaves
829 to millimetre waves. *Quarterly Journal of the Royal Meteorological Society*, *143*(702), 596-605.
830 <https://doi.org/10.1002/qj.2953>, 2017.

831 Rahimi, R., Ebtehaj, A., Panegrossi, G., Milani, L., Ringerud, S. E., & Turk, F. J., Vulnerability of Passive
832 Microwave Snowfall Retrievals to Physical Properties of Snowpack: A Perspective From Dense Media Radiative
833 Transfer Theory. *IEEE Transactions on Geoscience and Remote Sensing*, *60*, 1-13,
834 <https://doi.org/10.3390/rs11192200>, 2017.

835 Romanov, P.: Global multisensor automated satellite-based snow and ice mapping system (GMASI) for
836 cryosphere monitoring. *Remote Sensing of Environment*, *196*, 42-55, <https://doi.org/10.1016/j.rse.2017.04.023>,
837 2017.

838 Rosenkranz, P. W., Water vapor microwave continuum absorption: A comparison of measurements and models.
839 *Radio Science*, *33*(4), 919-928. <https://doi.org/10.1029/98RS01182>, 1998.

840 Rysman, J. F., Panegrossi, G., Sanò, P., Marra, A. C., Dietrich, S., Milani, L., & Kulie, M. S.: SLALOM: An all-
841 surface snow water path retrieval algorithm for the GPM Microwave Imager. *Remote Sensing*, *10*(8), 1278,
842 <https://doi.org/10.3390/rs10081278>, 2018.

843 Rysman, J. F., Panegrossi, G., Sano, P., Marra, A. C., Dietrich, S., Milani, L., Kulie, M. S., Casella, D., Camplani,
844 A., Claud, C., & Edel, L.: Retrieving surface snowfall with the GPM Microwave Imager: A new module for the
845 SLALOM algorithm. *Geophysical Research Letters*, *46*(22), 13593-13601,
846 <https://doi.org/10.1029/2019GL084576>, 2019.

847 Sanò, P., Casella, D., Camplani, A., D'Adderio, L. P., & Panegrossi, G., A Machine Learning Snowfall Retrieval
848 Algorithm for ATMS. *Remote Sensing*, *14*(6), 1467, <https://doi.org/10.3390/rs14061467>, 2022.

849 Sanò, P., Panegrossi, G., Casella, D., Di Paola, F., Milani, L., Mugnai, A., Petracca, M., & Dietrich, S. (2015).
850 The Passive microwave Neural network Precipitation Retrieval (PNPR) algorithm for AMSU/MHS observations:
851 description and application to European case studies. *Atmospheric Measurement Techniques*, *8*(2), 837-857,
852 <https://doi.org/10.5194/amt-8-837-2015>, 2015.

853 Skofronick-Jackson, G. M., Kim, M. J., Weinman, J. A., & Chang, D. E. (2004). A physical model to determine
854 snowfall over land by microwave radiometry. *IEEE Transactions on Geoscience and Remote Sensing*, *42*(5),
855 1047-1058, DOI:10.1109/TGRS.2004.825585, 2004.

856 Skofronick-Jackson, G., Hudak, D., Petersen, W., Nesbitt, S. W., Chandrasekar, V., Durden, S., Kristin, J. G.,
857 Huang, G., Joe, P., Kollias, P., Reed, K., A., Schwaller, M., R., Stewart, R., Tanelli, S., Tokay, A., Wang, J., R.,
858 & Wolde, M.: Global precipitation measurement cold season precipitation experiment (GCPEX): For
859 measurement's sake, let it snow. *Bulletin of the American Meteorological Society*, *96*(10), 1719-1741,
860 <https://doi.org/10.1175/BAMS-D-13-00262.1>, 2015.

861 Stephens, G. L., Vane, D. G., Tanelli, S., Im, E., Durden, S., Rokey, M., Reinke, D., Partain, P., Mace, G. G.,
862 Austin, R., L'Ecuyer, T., Haynes, J., Lebsock, M., Suzuki, K., Waliser, D., Wu, D., Kay, J., Gettelman, A., Zhien
863 Wang, Z., & Marchand, R.: CloudSat mission: Performance and early science after the first year of operation.
864 *Journal of Geophysical Research: Atmospheres*, *113*(D8), <https://doi.org/10.1029/2008JD009982>, 2008.

865 Takbiri, Z., Ebtehaj, A., Fofoula-Georgiou, E., Kirstetter, P. E., & Turk, F. J.: A prognostic nested k-nearest
866 approach for microwave precipitation phase detection over snow cover. *Journal of hydrometeorology*, *20*(2), 251-
867 274, <https://doi.org/10.1175/JHM-D-18-0021.1>, 2019.

868 Turk, F. J., Ringerud, S. E., Camplani, A., Casella, D., Chase, R. J., Ebtehaj, A., Gong, J., Kulie, M., Liu, G.,
869 Milani, L., Panegrossi, G., Padullés, R., Rysman, J. F., Sanò, P., Vahedizade, S., & Wood, N. B.: Applications of
870 a CloudSat-TRMM and CloudSat-GPM satellite coincidence dataset. *Remote Sensing*, *13*(12), 2264,
871 <https://doi.org/10.3390/rs13122264>, 2021a.

872 Turk, F. J., Ringerud, S. E., You, Y., Camplani, A., Casella, D., Panegrossi, G., Sanò, P., Ebtehaj, A., Guilloteau,
873 C., Utsumi, N., Prigent, C., & Peters-Lidard, C.: Adapting passive microwave-based precipitation algorithms to

874 variable microwave land surface emissivity to improve precipitation estimation from the GPM constellation.
875 *Journal of Hydrometeorology*, 22(7), 1755-1781, <https://doi.org/10.1175/JHM-D-20-0296.1>, 2021.

876 Ulaby, F., & Long, D., Microwave radar and radiometric remote sensing, 1st Edition, the Univ. of Michigan Press,
877 ISBN: 978-0-472-11935-6, 2014.

878 Vihma, T., Screen, J., Tjernström, M., Newton, B., Zhang, X., Popova, V., Deser, C., Holland, M., & Prowse, T.:
879 The atmospheric role in the Arctic water cycle: A review on processes, past and future changes, and their impacts.
880 *Journal of Geophysical Research: Biogeosciences*, 121(3), 586-620, <https://doi.org/10.1002/2015JG003132>,
881 2016.

882 Wang, Y., Liu, G., Seo, E. K., & Fu, Y.: Liquid water in snowing clouds: Implications for satellite remote sensing
883 of snowfall. *Atmospheric research*, 131, 60-72, <https://doi.org/10.1016/j.atmosres.2012.06.008>, 2013.

884 Weng, F., Zou, X., Wang, X., Yang, S., & Goldberg, M. D.: Introduction to Suomi national polar-orbiting
885 partnership advanced technology microwave sounder for numerical weather prediction and tropical cyclone
886 applications. *Journal of geophysical research: atmospheres*, 117(D19), <https://doi.org/10.1029/2012JD018144>,
887 2012.

888 Wood, N. B. and T. S. L'Ecuyer: Level 2C Snow Profile Process Description and Interface Control Document,
889 Product Version P1 R05. NASA JPL CloudSat project document revision 0., 26 pp, Available from
890 [https://www.cloudsat.cira.colostate.edu/cloudsat-static/info/dl/2c-snow-profile/2C-SNOW-](https://www.cloudsat.cira.colostate.edu/cloudsat-static/info/dl/2c-snow-profile/2C-SNOW-PROFILE_PDICD.P1_R05.rev0_.pdf)
891 [PROFILE_PDICD.P1_R05.rev0_.pdf](https://www.cloudsat.cira.colostate.edu/cloudsat-static/info/dl/2c-snow-profile/2C-SNOW-PROFILE_PDICD.P1_R05.rev0_.pdf)[https://www.cloudsat.cira.colostate.edu/cloudsat-static/info/dl/2c-snow-](https://www.cloudsat.cira.colostate.edu/cloudsat-static/info/dl/2c-snow-profile/2C-SNOW-PROFILE_PDICD.P1_R05.rev0_.pdf)
892 [profile/2C-SNOW-PROFILE_PDICD.P1_R05.rev0_.pdf](https://www.cloudsat.cira.colostate.edu/cloudsat-static/info/dl/2c-snow-profile/2C-SNOW-PROFILE_PDICD.P1_R05.rev0_.pdf), 2018.

893 You, Y., Meng, H., Dong, J., Fan, Y., Ferraro, R. R., Gu, G., & Wang, L.: A Snowfall Detection Algorithm for
894 ATMS Over Ocean, Sea Ice, and Coast. *IEEE Journal of Selected Topics in Applied Earth Observations and*
895 *Remote Sensing*, 15, 1411-1420, DOI:[10.1109/JSTARS.2022.3140768](https://doi.org/10.1109/JSTARS.2022.3140768), 2022.

896 You, Y., Meng, H., Dong, J., & Rudlosky, S.: Time-lag correlation between passive microwave measurements
897 and surface precipitation and its impact on precipitation retrieval evaluation. *Geophysical Research Letters*,
898 46(14), 8415-8423, doi: 10.1029/2019GL083426, 2019.

899 Zhao, L., & Weng, F.: Retrieval of ice cloud parameters using the Advanced Microwave Sounding Unit. *Journal*
900 *of Applied Meteorology and Climatology*, 41(4), 384-395, <https://www.jstor.org/stable/26184983>, 2002.

901
902
903
904
905
906
907
908
909
910
911
912
913
914
915
916

Figures

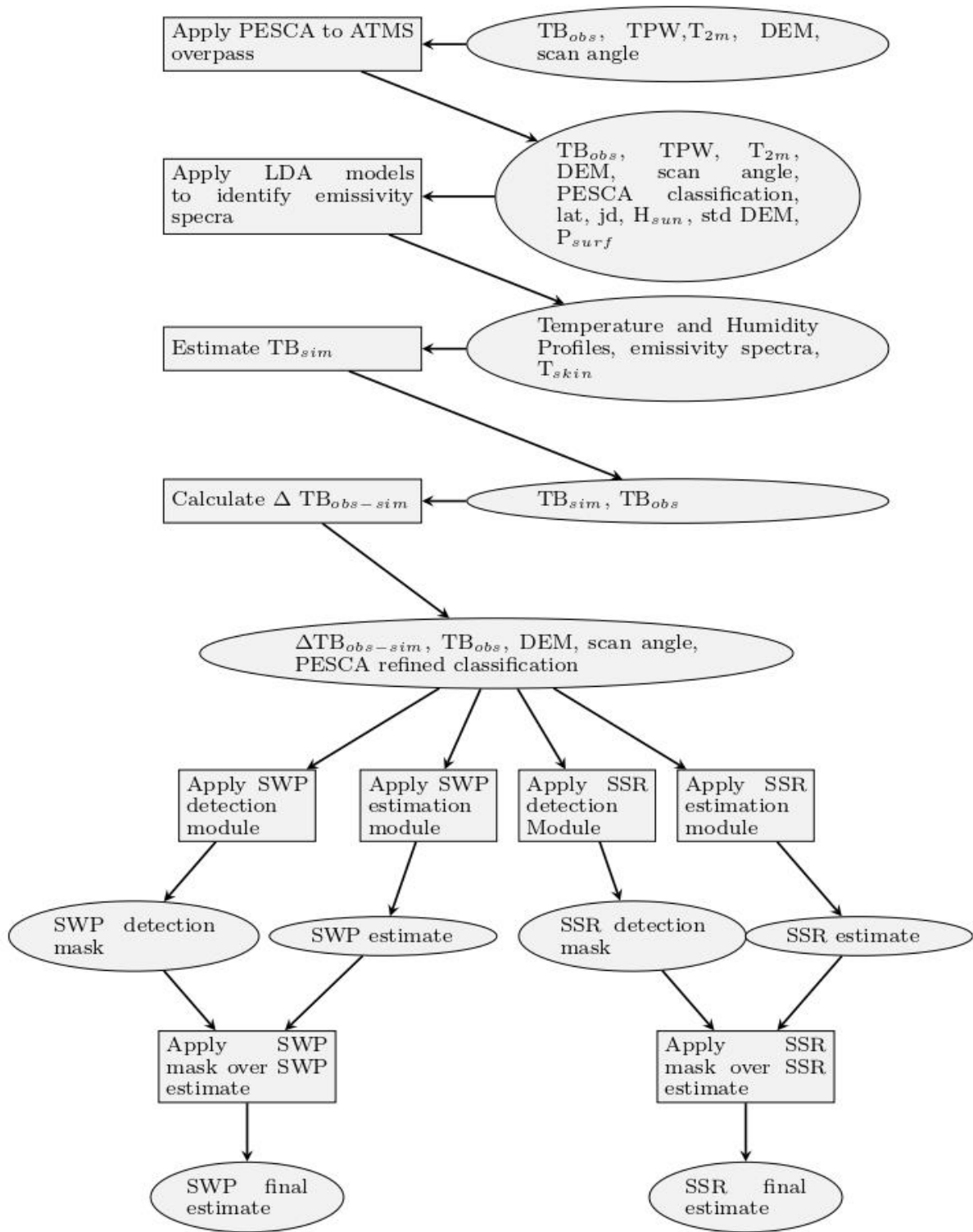
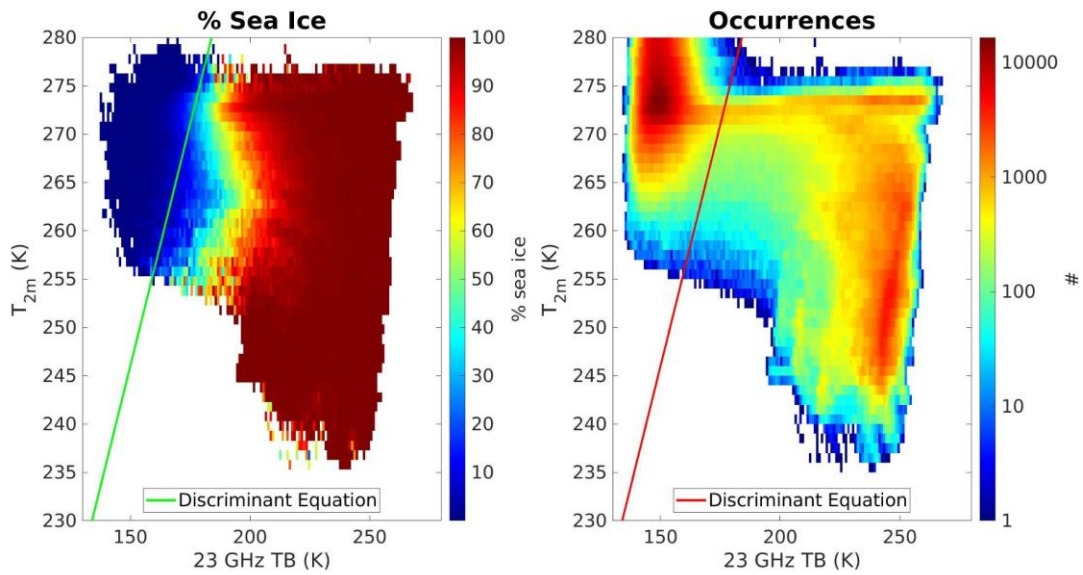


Figure 1: HANDEL-ATMS workflow diagram (please, refer to the text for details)

917
918
919



920
 921
 922
 923
 924

Figure 2: Sea Ice detection representation on a 23 GHz TB- T_{2m} Plane. The color represents the mean AutoSnow sea ice percentage within each bin (left) and the observation occurrence (right). The green (left) and red (right) lines represent the discriminant Equation (Equation 1) between sea ice and ocean.

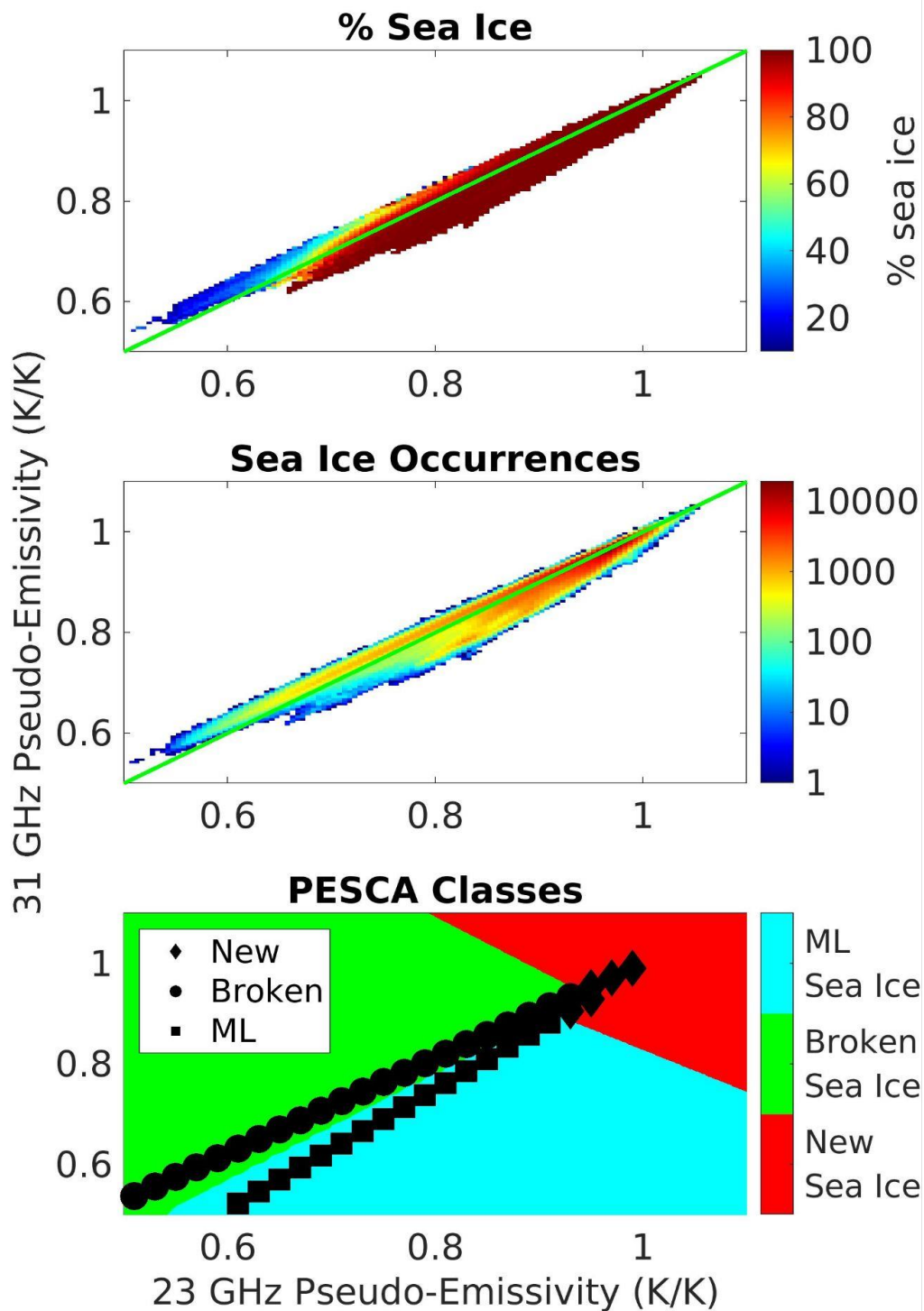
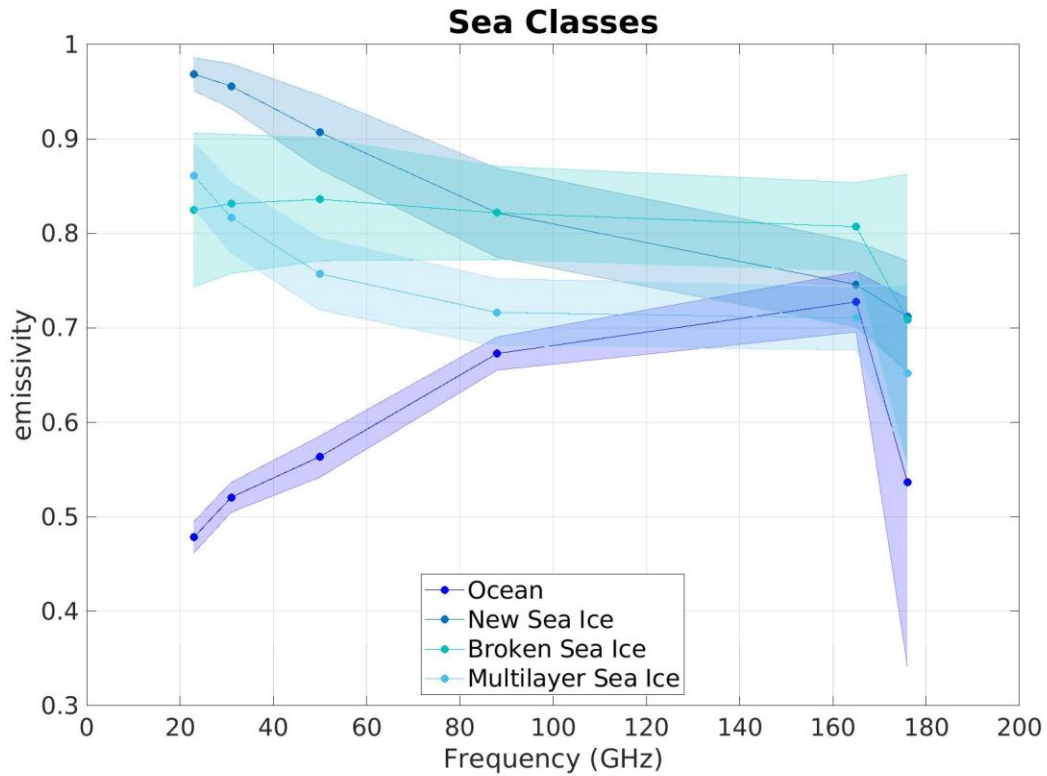


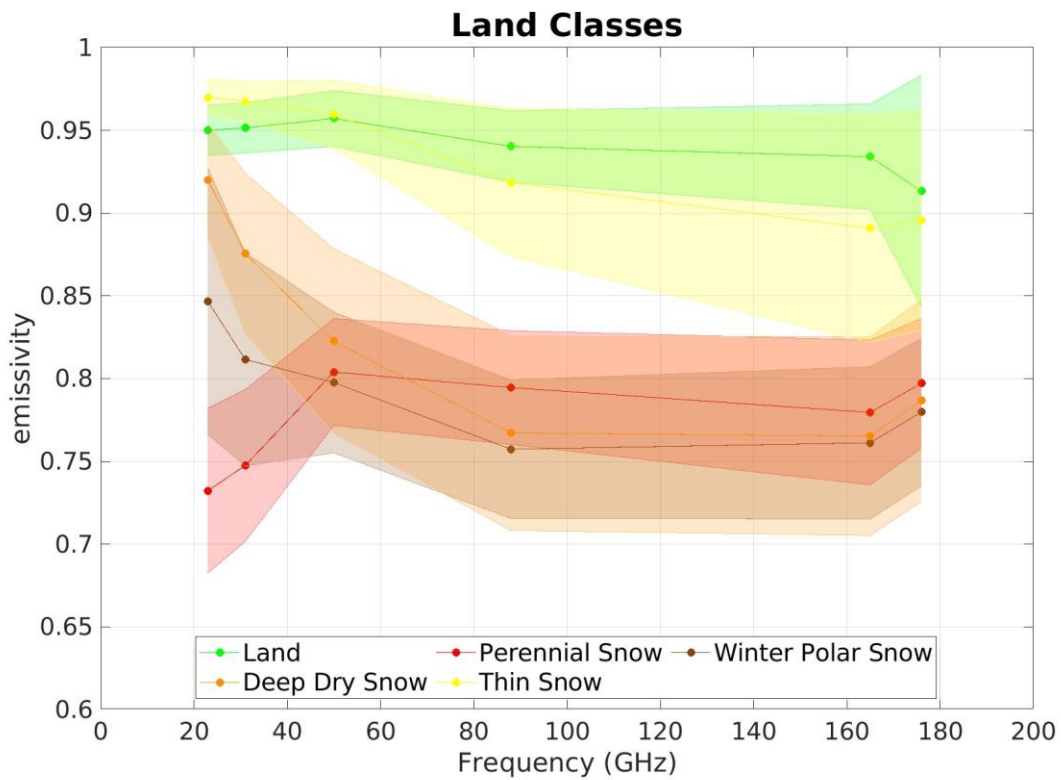
Figure 3: Sea Ice detection and classification: relationship between 31 GHz Pseudo-Emissivity (y-axis) and 23 GHz Pseudo-Emissivity (x-axis). The color represents the mean AutoSnow sea ice percentage within each bin (top panel), the observation occurrence (middle panel), and the PESCA classification (Multi-Layer (ML), Broken and New ~~sea-ice~~Sea Ice) with the Nearest Neighbor markers (bottom panel). The green continuous lines at the top and the center panels represent the bisector.

925
926
927
928
929
930
931



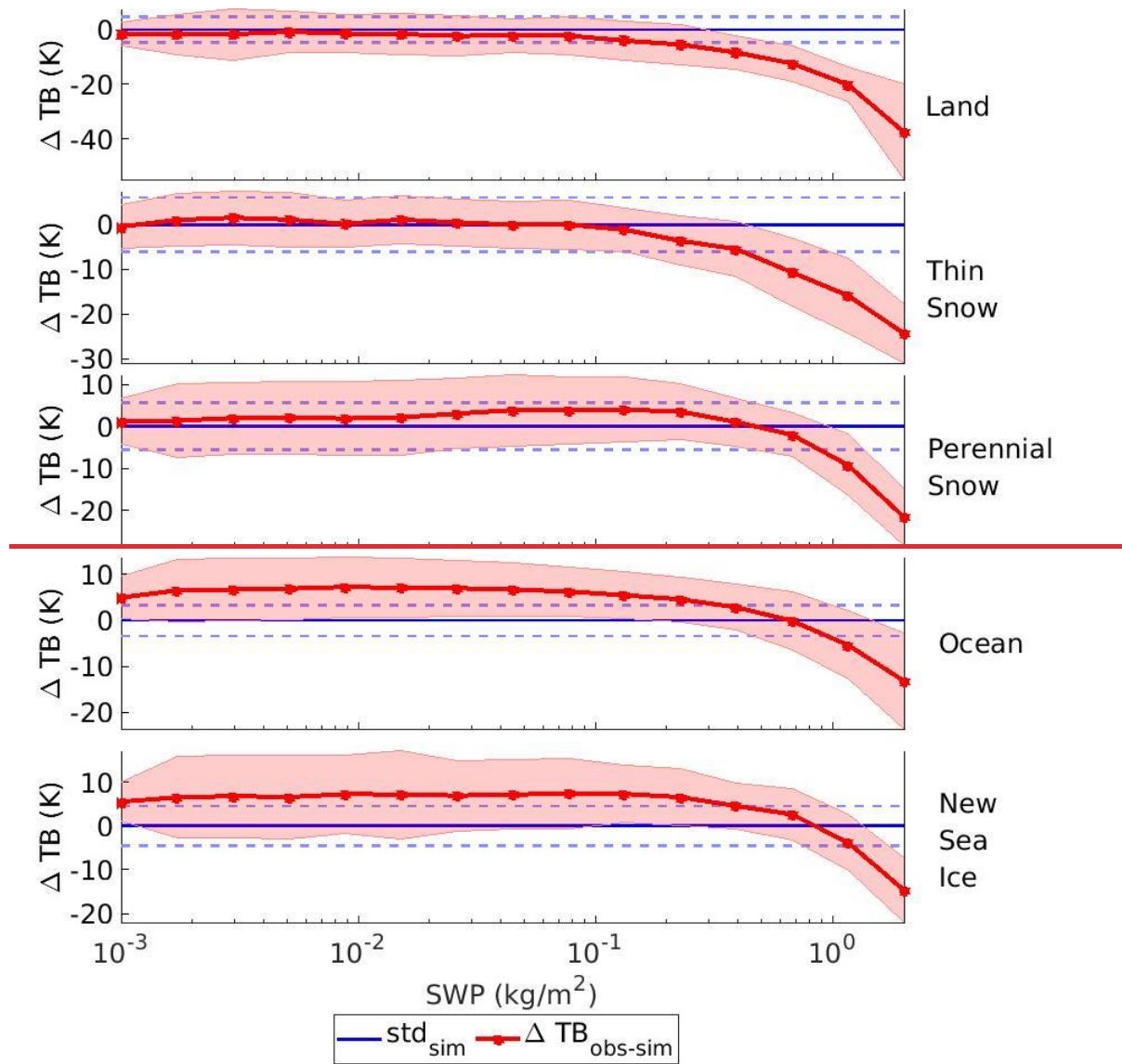
932
933
934
935

Figure 4: Emissivity Spectra for PESCA Sea Classes. The continuous lines represent the mean values of the emissivity while the shaded areas represent the standard deviation calculated at the ATMS reference frequencies (23.8 GHz, 31.4 GHz, 50.3 GHz, 88.2 GHz, 165.5 GHz, and 183.3 ±7 GHz) represented by the dots.

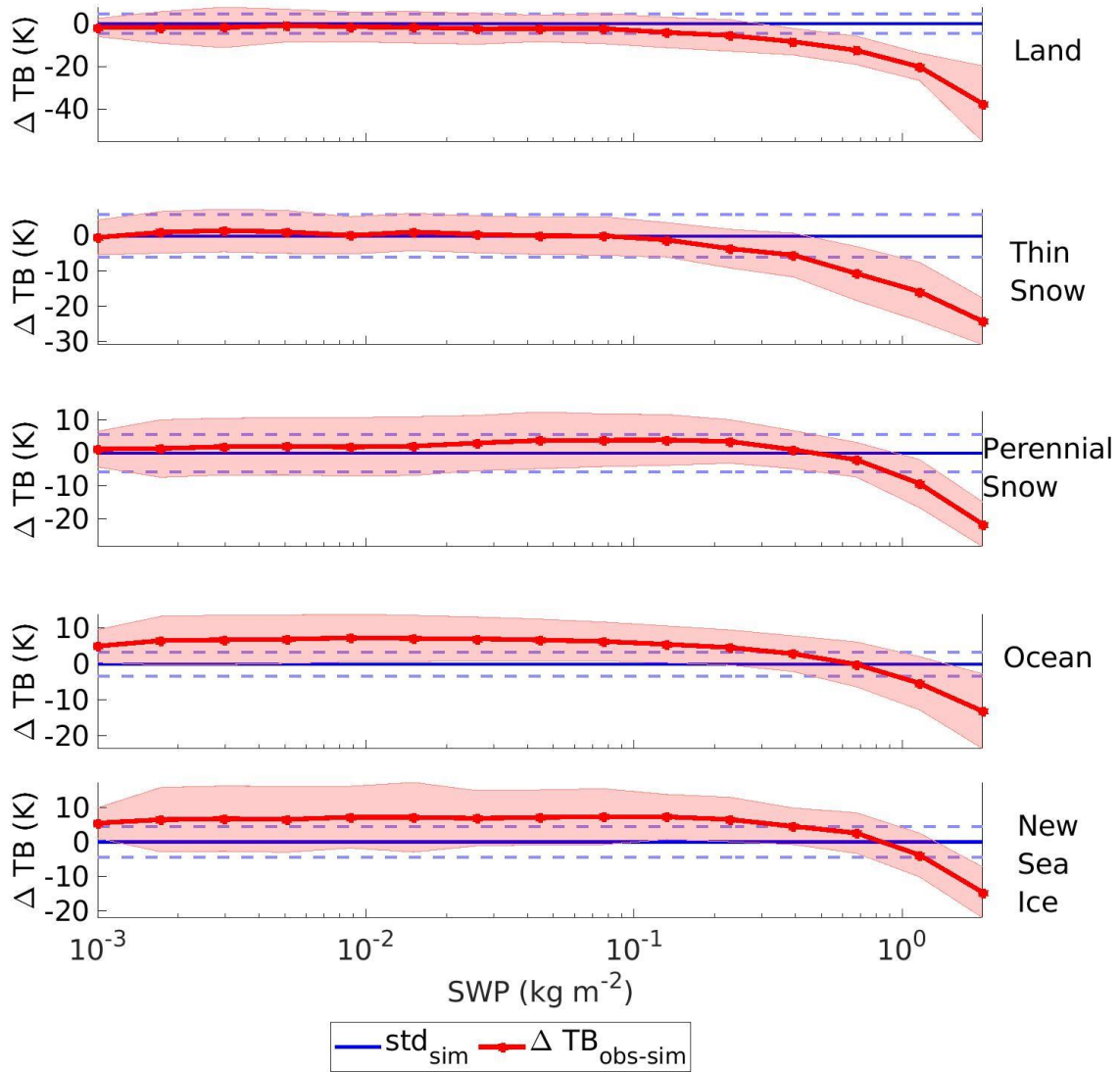


936
937

Figure 5: Same as Figure 4 but for PESCA Land Classes.

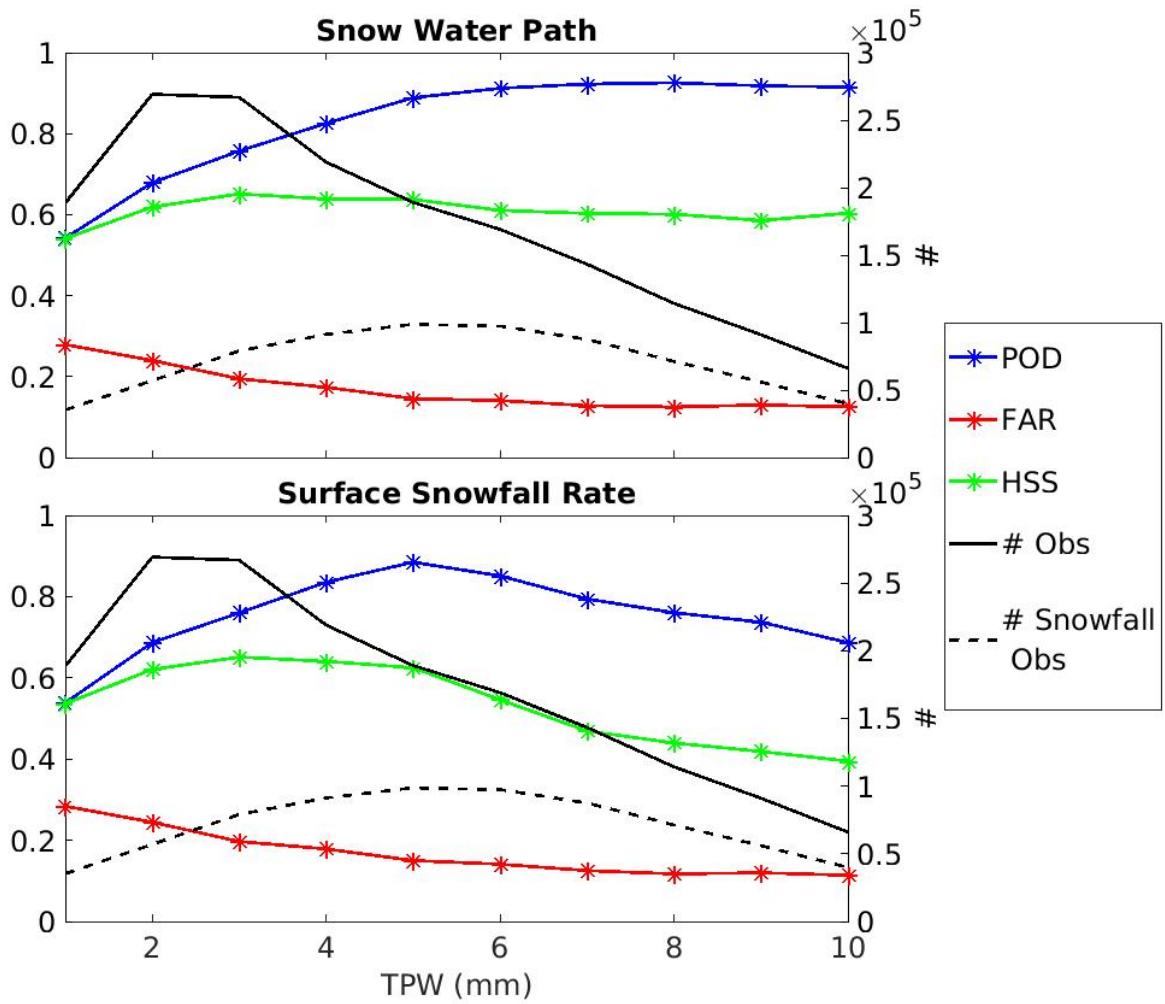


938



939
 940
 941
 942
 943

Figure 6: Snowfall Signature at 165.5 GHz as a function of SWP for five PESCA surface classes. The red line and shaded areas represent the mean values and standard deviations of $\Delta TB_{\text{obs-sim}}$ (i.e., the snowfall signature) while the blue lines are centered on the estimated bias and standard deviation of $\Delta TB_{\text{obs-sim}}$ in clear sky conditions for the corresponding PESCA surface class.



944

945

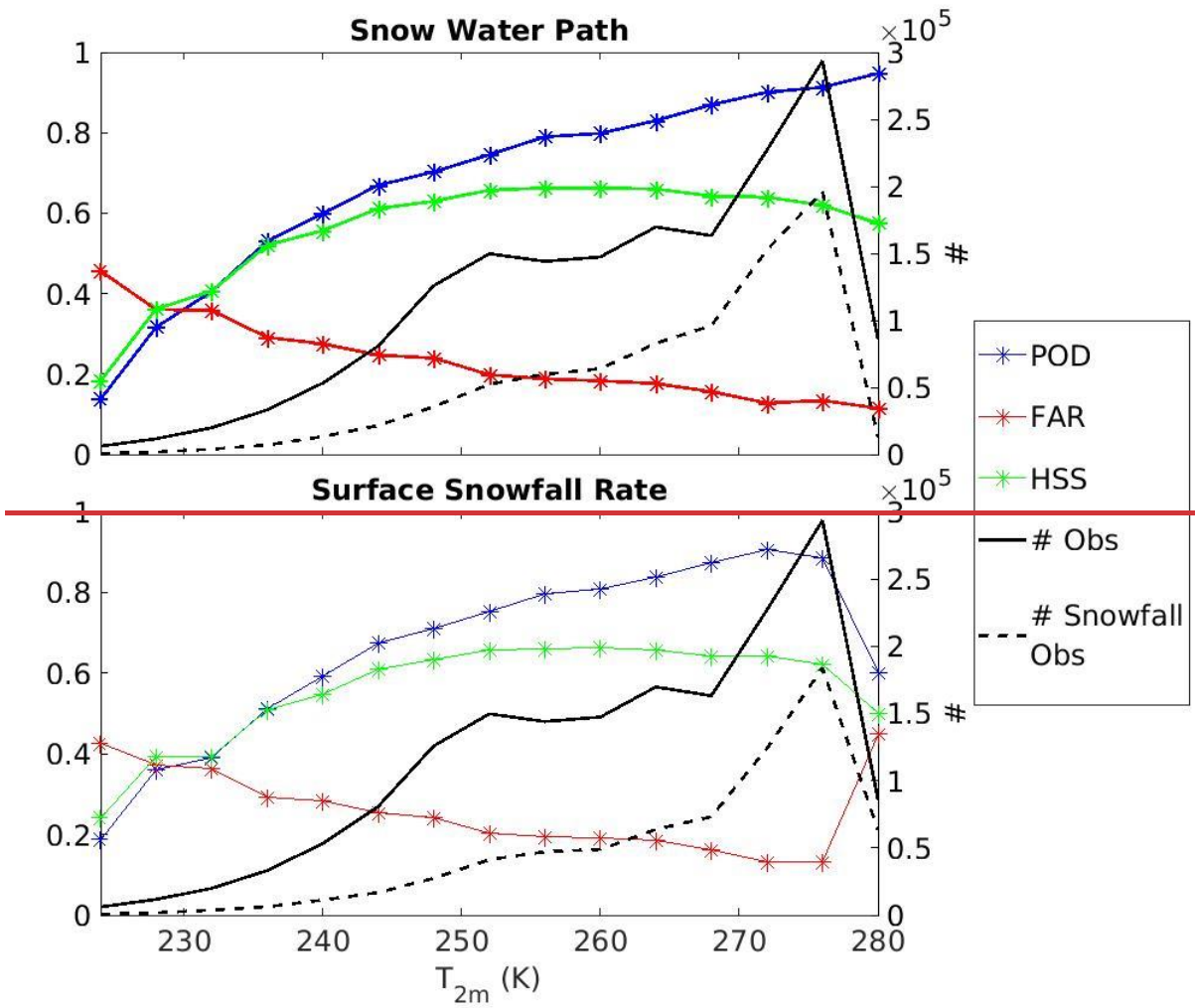
946

947

948

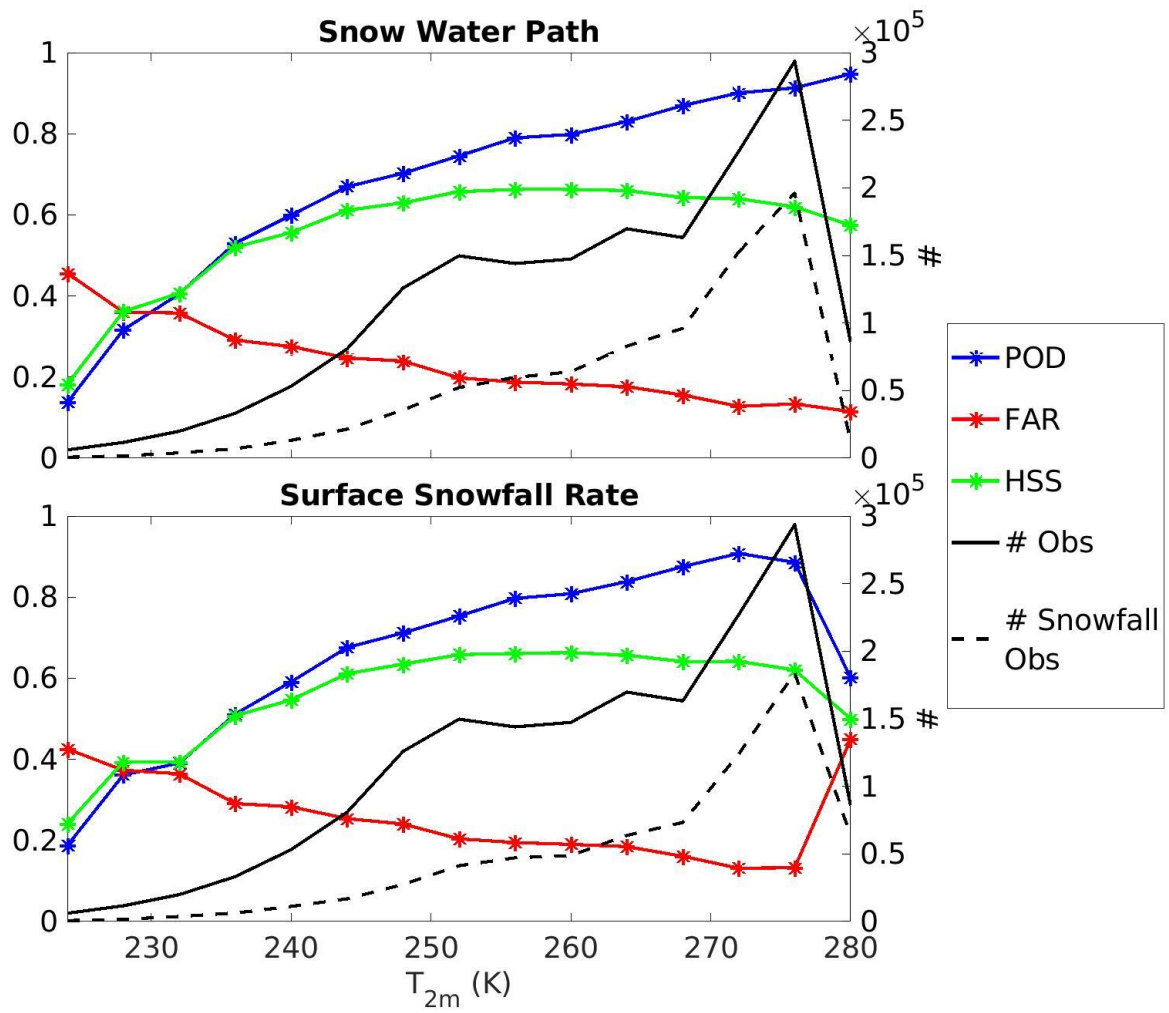
949

Figure 7: Dependence of HANDEL-ATMS SWP and SSR detection statistical scores on TPW, calculated for the test dataset. Each star represents the statistical score value for different 1-mm bin of TPW. The left y-axis reports POD, FAR and HSS values, while the right y-axis reports the number of total and snowfall observations in the validationtest dataset.



950

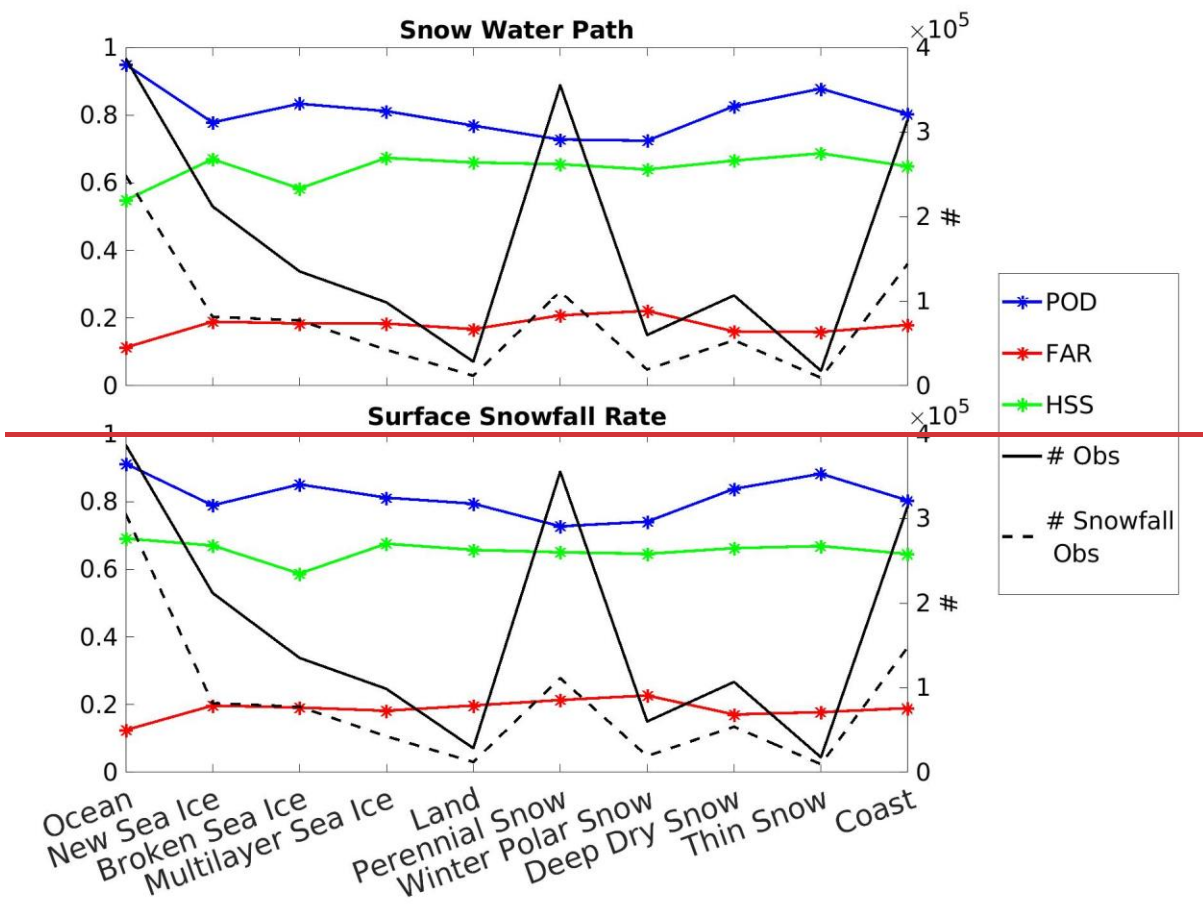
951



952

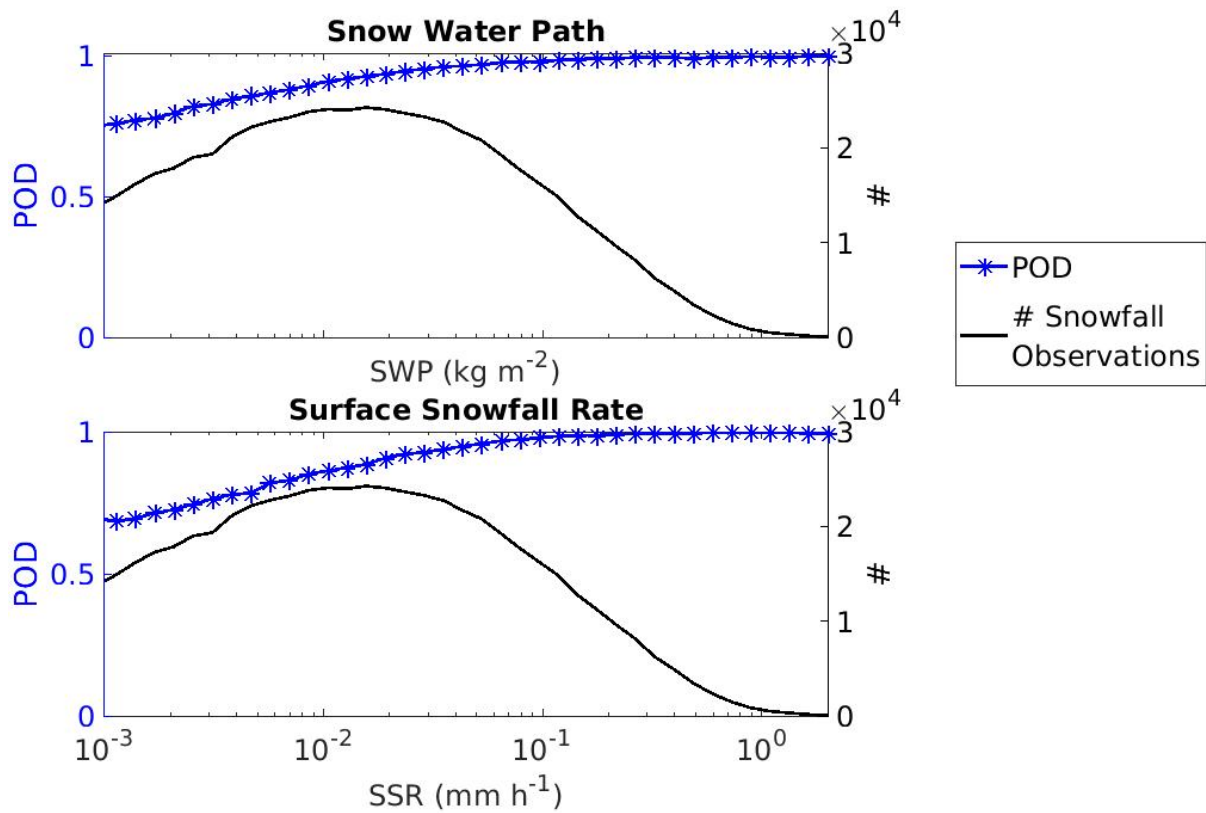
953

Figure 8: Same as Figure 7 but for T_{2m} bins.



954

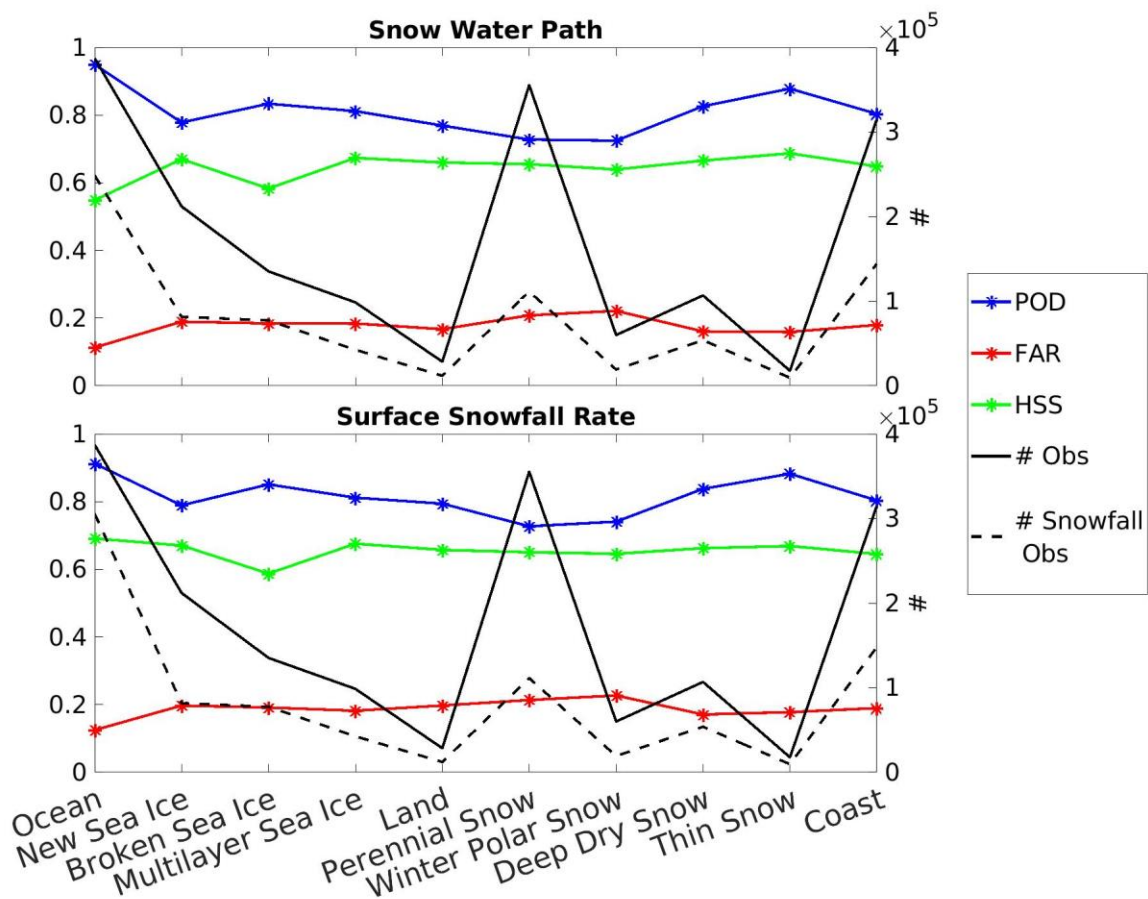
955



956

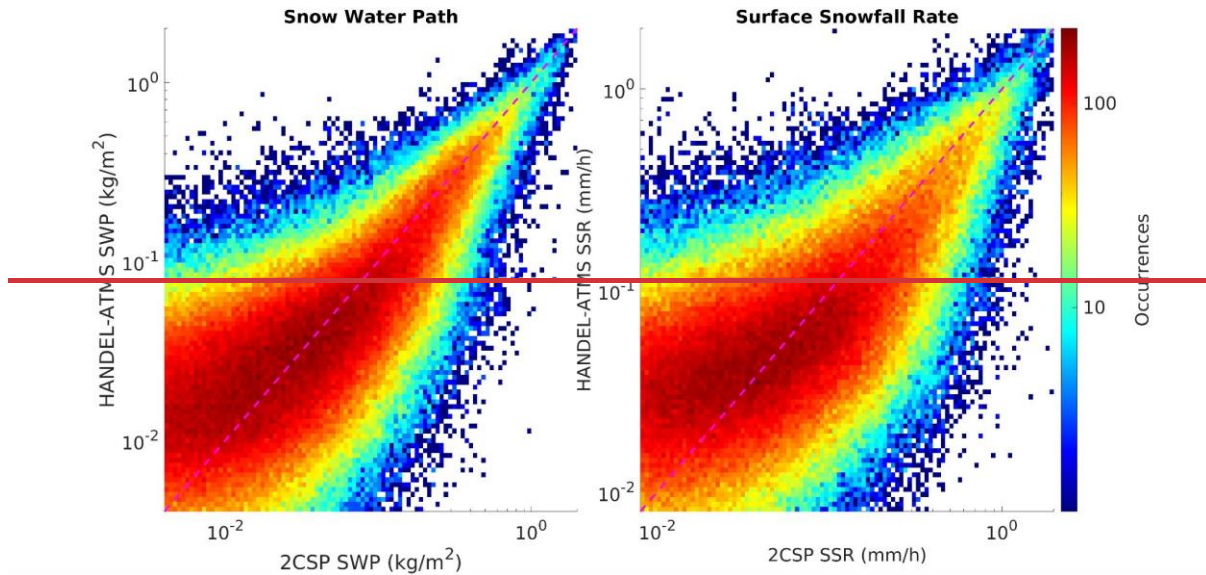
957 Figure 9: Dependence of HANDEL-ATMS SWP and SSR POD on SWP/SSR values. Each star represents the
958 statistical score value for different SWP/SSR bins. The left y-axis reports POD values, while the right y-axis
959 reports the number of snowfall observations in the test dataset. Only POD has been reported because the
960 index has been calculated for observations where CPR 2CSP detects the presence of SWP/SSR.

961

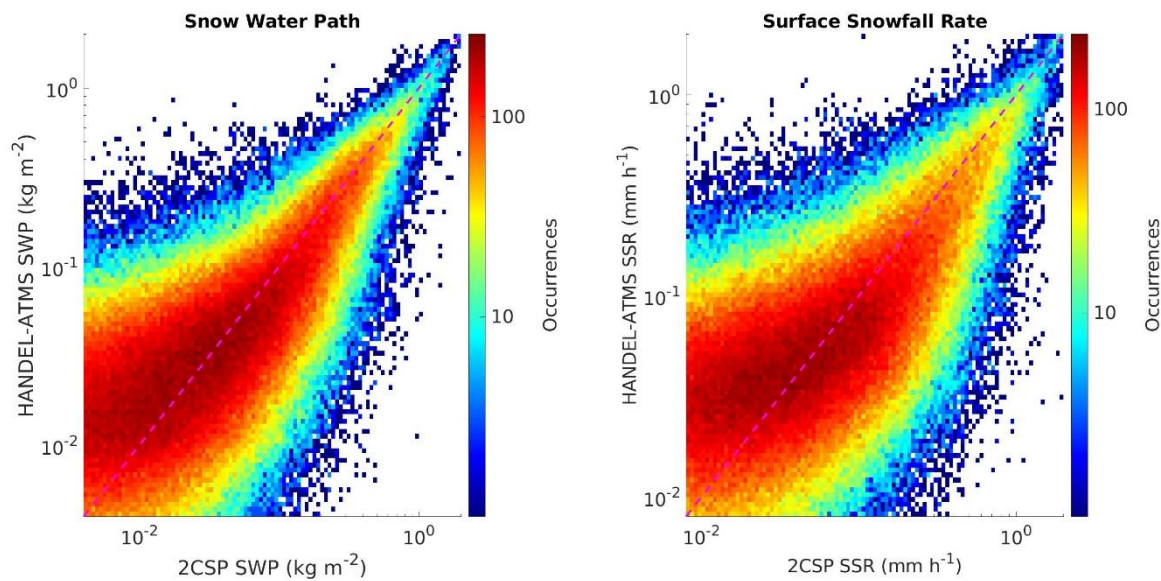


962
 963
 964
 965

Figure 10: Same as Figure 7 but for PESCA surface classes. Each star represents the value of the statistical score for each surface category.



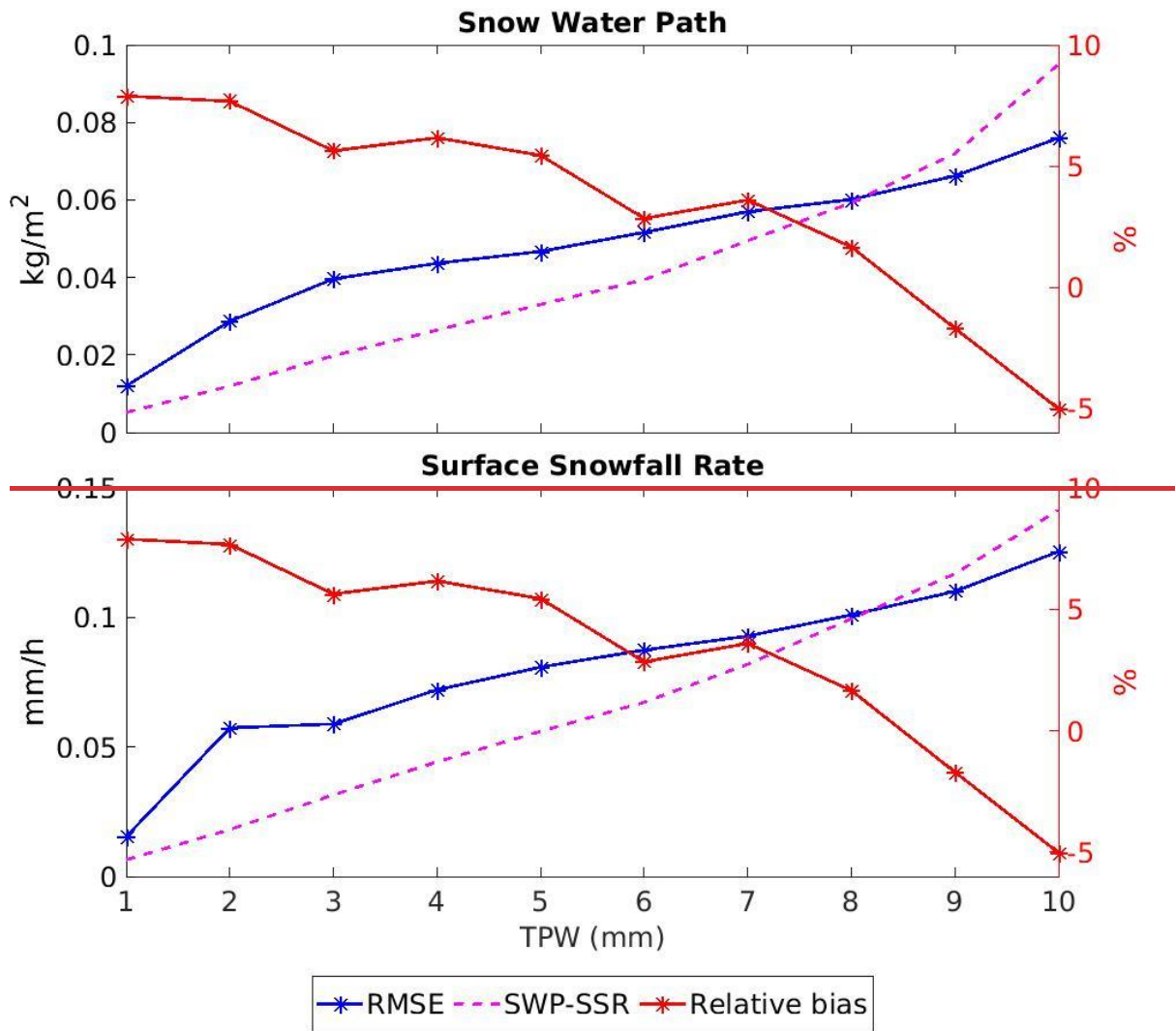
966
967



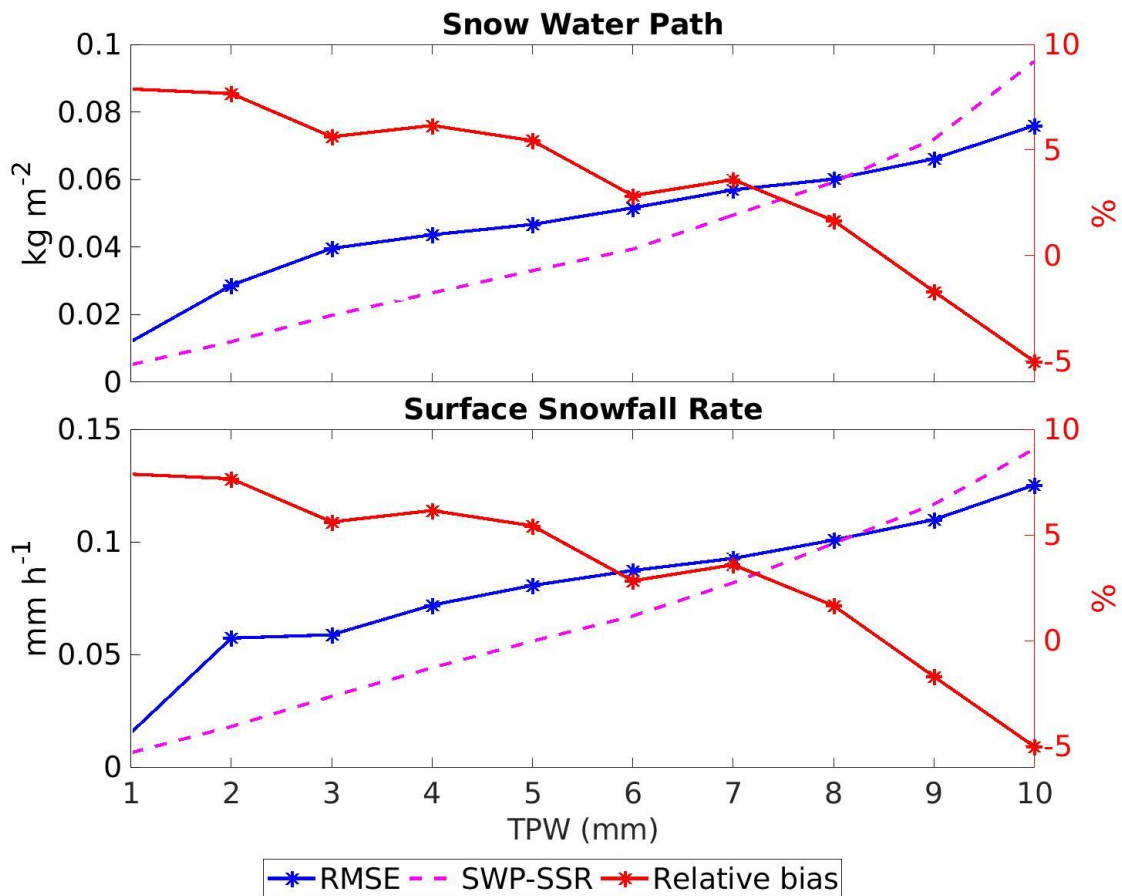
968
969
970
971
972

Figure 1011: 2D Histogram reporting HANDEL-ATMS SWP (left) and SSR (right) estimation (y-axis) and 2CSP estimation (x-axis). The colorbar represents the number of observations for each HANDEL-ATMS/2CSP bin. (test dataset). The violet dashed line represents the bisector.

973

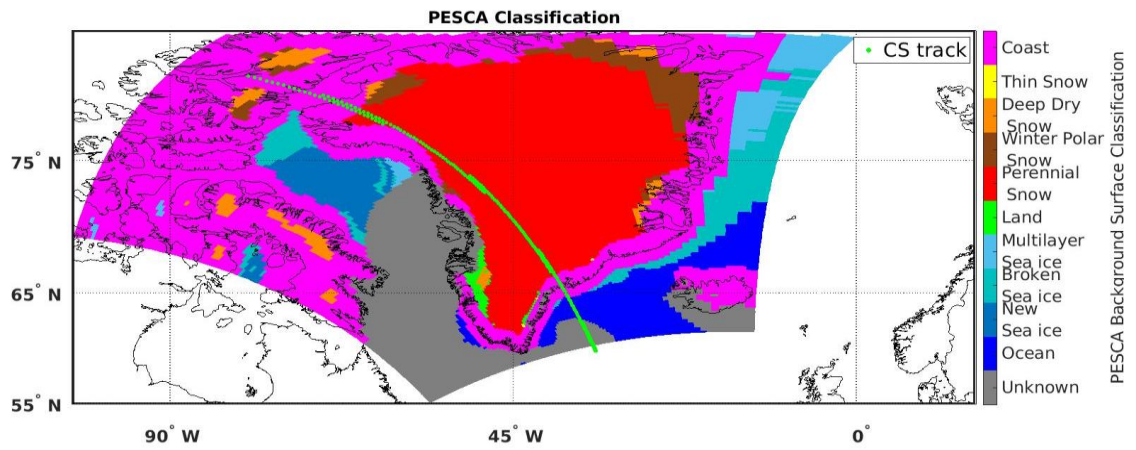


974
975
976



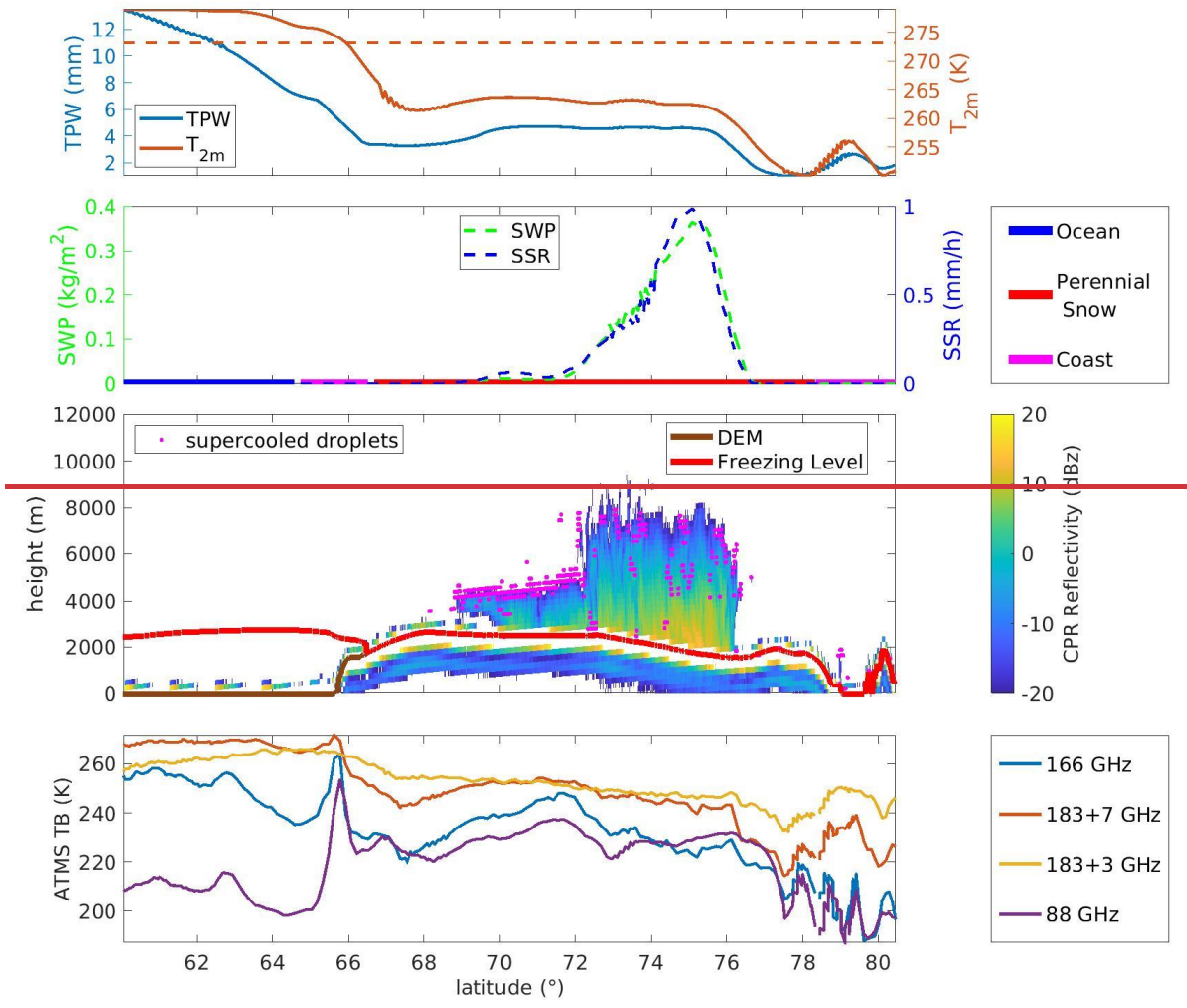
977
978
979
980
981
982
983

Figure 14.12: Dependence of HANDEL-ATMS SWP and SSR estimation on TPW calculated for the test dataset. Each star represents the value of the statistical score for different 1-mm TPW bins. The left y-axis reports the RMSE and the mean intensity SWP and SSR value for each 1-mm TPW bin, while the right y-axis reports the relative bias, calculated as the ratio between the bias and the SWP/SSR mean value for each bin.

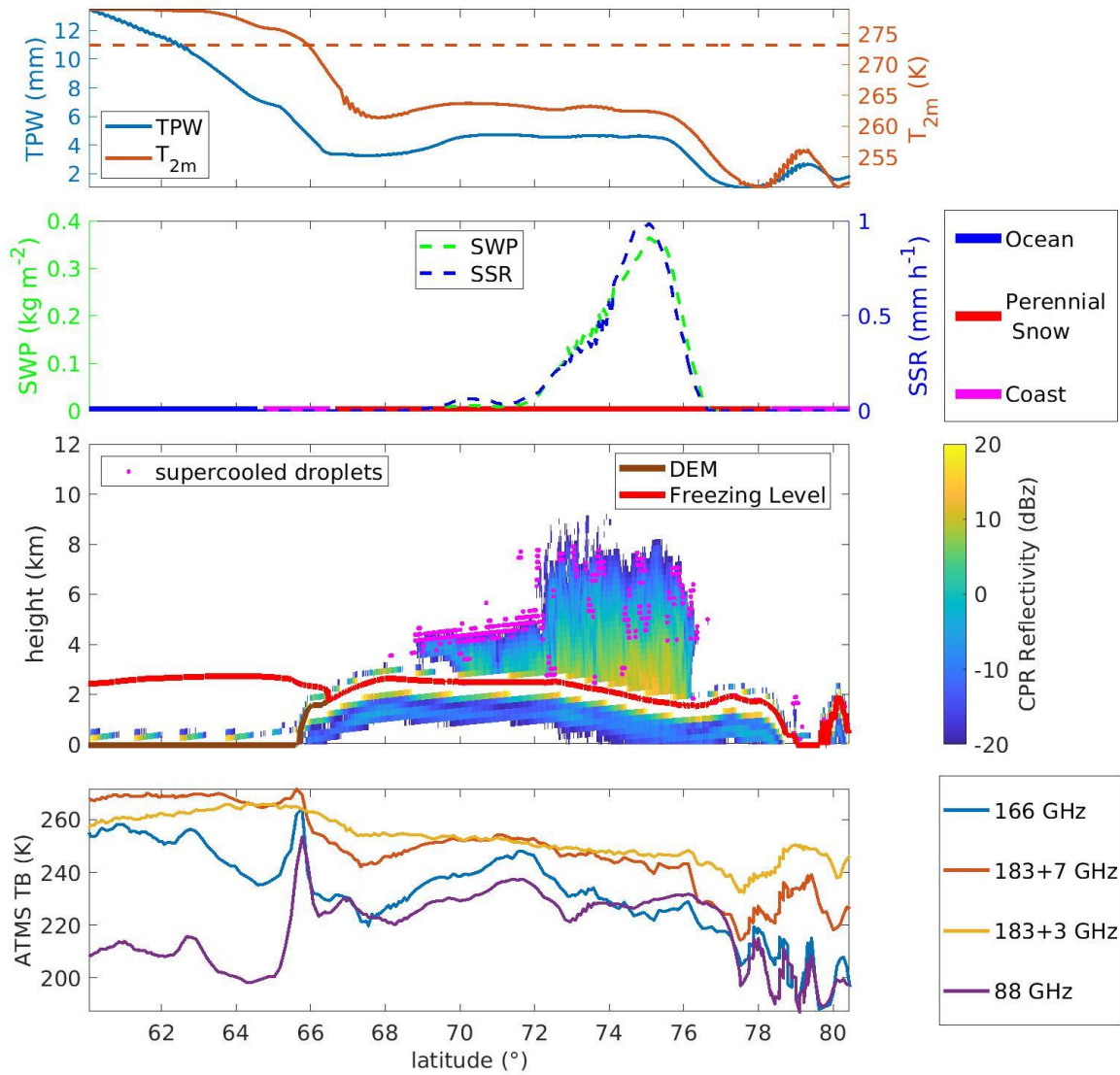


984
985
986
987
988
989

Figure 1213: Greenland - 2016/04/24 - ATMS overpass is between 14:54 UTC and 14:58 UTC, while the CPR overpass is between 15:05 UTC and 15:12 UTC. Map of the PESCA Background Surface Classification. The green dotted line represents the CloudSat track.



990



991

992

993

994

995

996

997

998

999

1000

1001

1002

1003

Figure 1314: Greenland - 2016/04/24 - Synopsis along CloudSat Track. First panel: ECMWF TPW and T_{2m} values along the CloudSat track. Second panel: the 2CSP SWP (left) and the SSR (right), and the PESCA classification along CloudSat track. Third panel: CPR reflectivity (values are reported in the colorbar on the right), and supercooled water droplets detected by DARDAR (magenta points), Digital Elevation Model (brown line) and the ECMWF Freezing Level (red line) along CloudSat track. Bottom panel: the ATMS TBs of the high-frequency channels (88 GHz, 166 GHz, 183+3 GHz, 183+7 GHz) along CloudSat track.

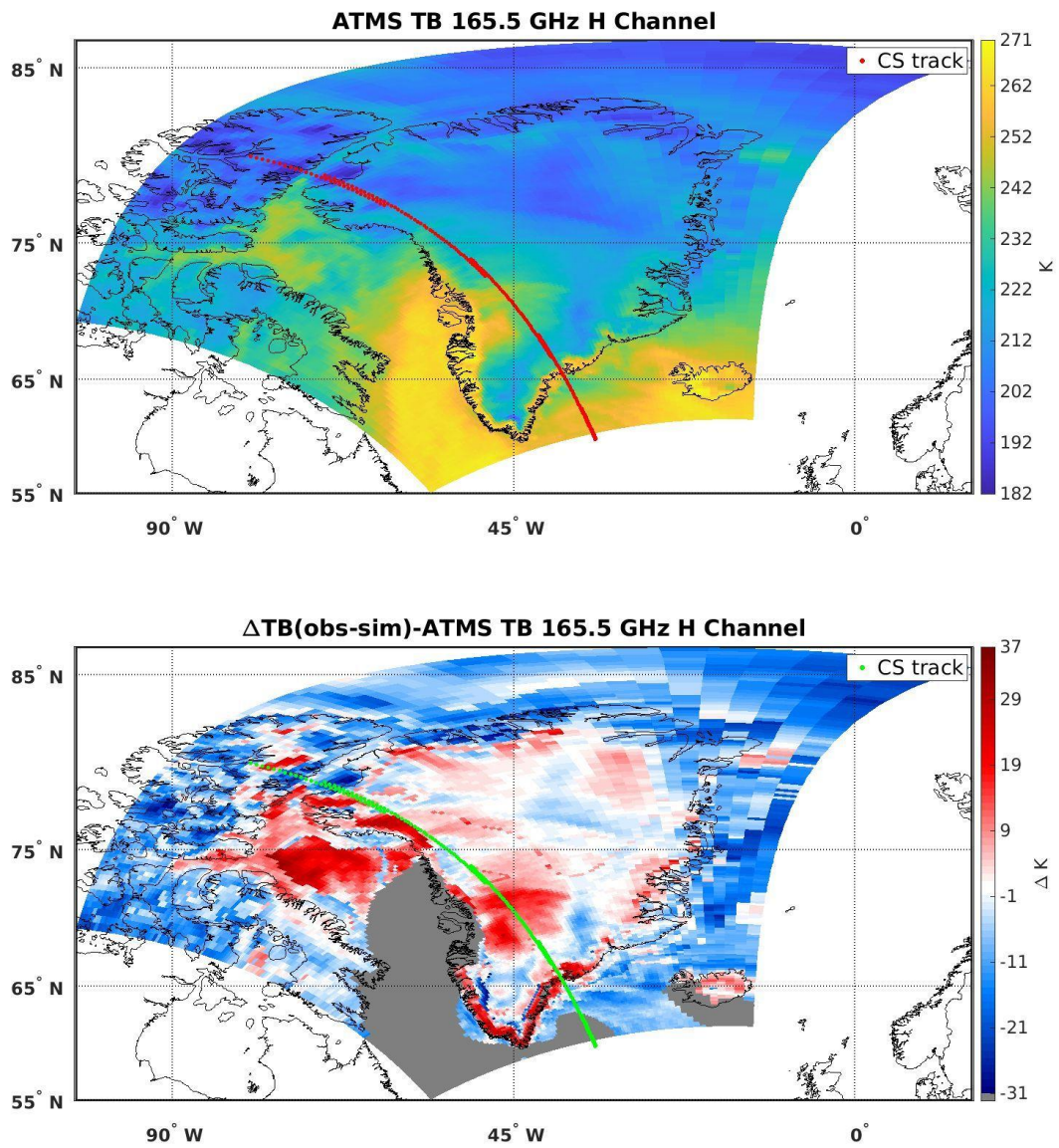
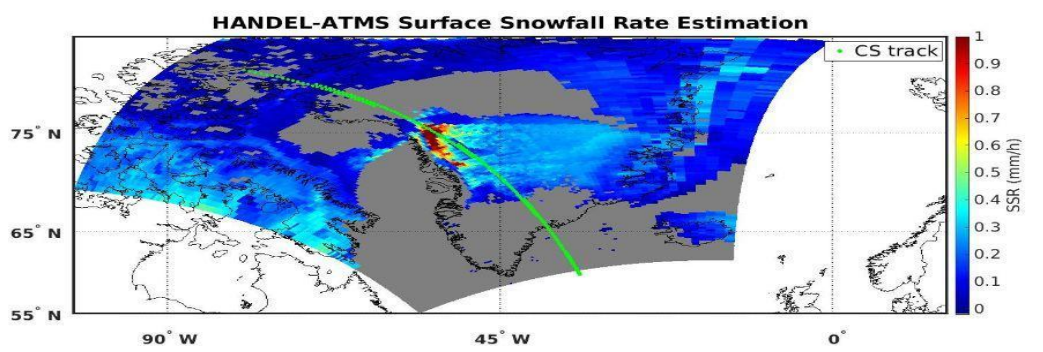
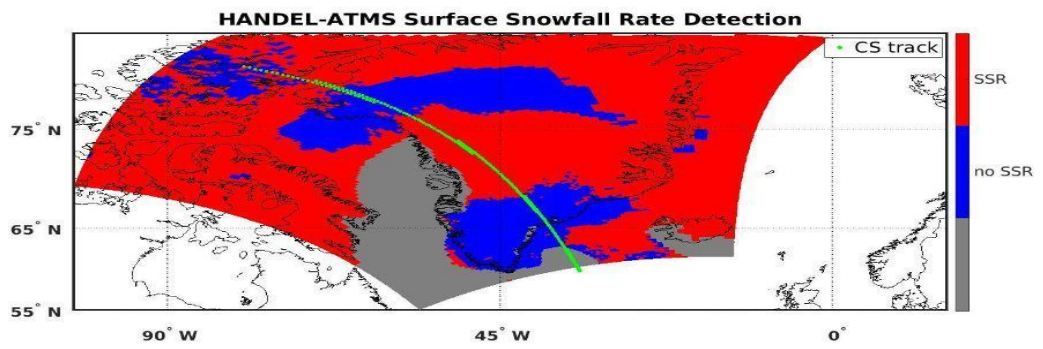
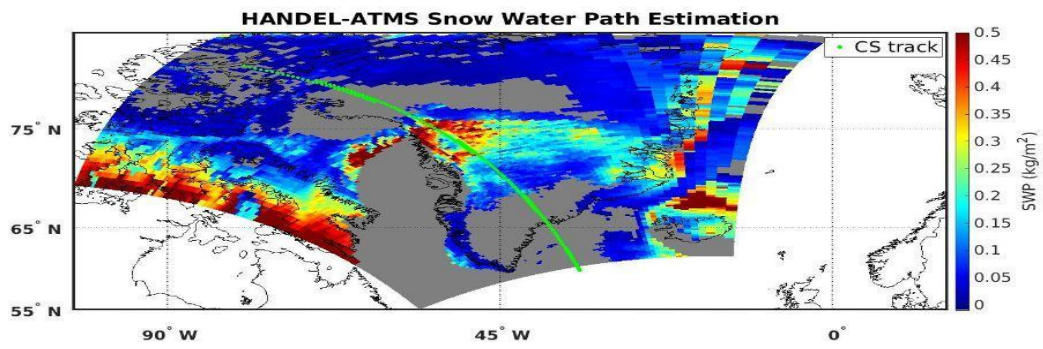
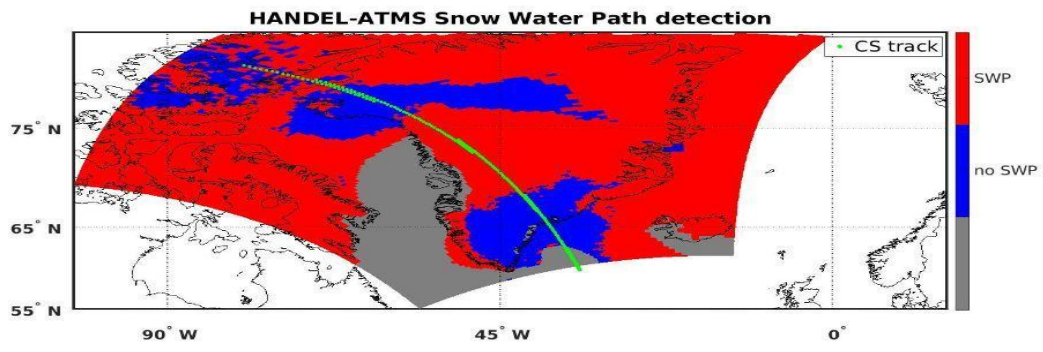
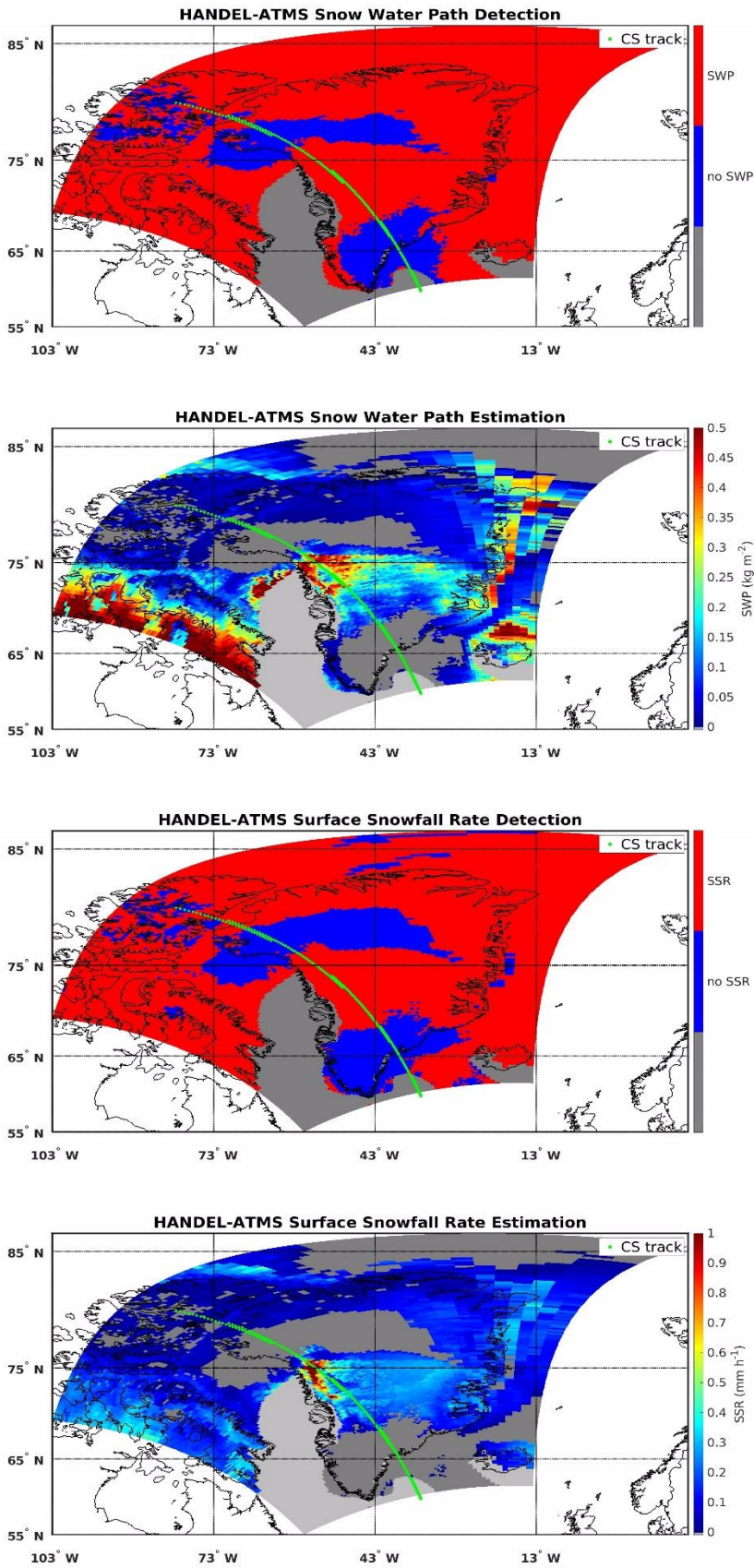


Figure 4415: Greenland - 2016/04/24 - 165 GHz Channel measured TB (TB_{obs}) (top panel) and the deviation of TB_{obs} from the simulated clear-sky TBs ($\Delta TB_{\text{obs-sim}}$) (bottom panel). The red dotted line (top panel) and the green dotted line (bottom panel) represent the CloudSat track.

1004
 1005
 1006
 1007
 1008
 1009

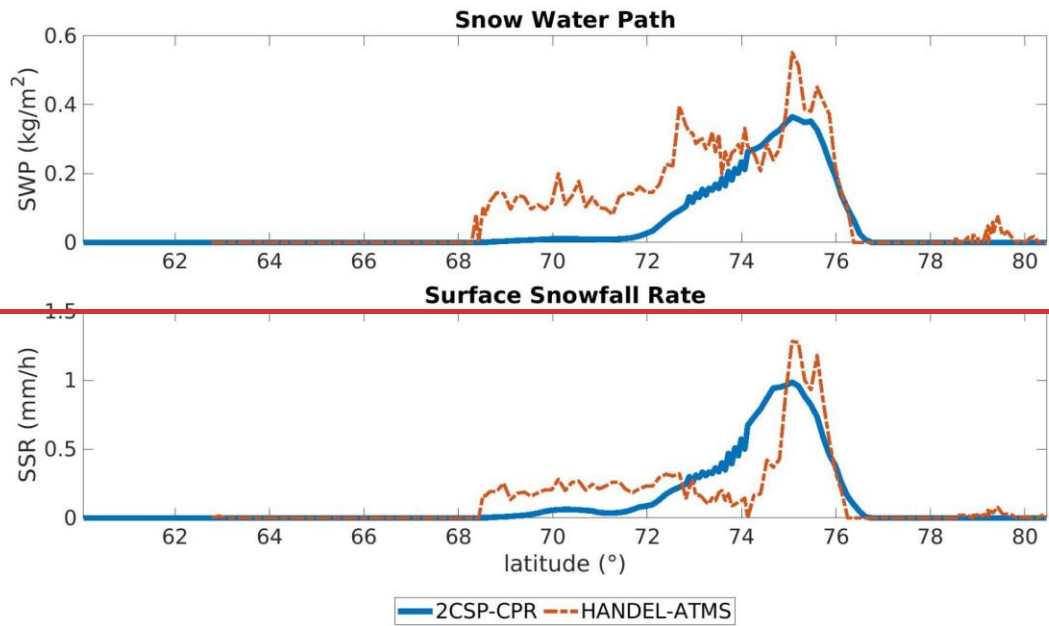




1011
 1012
 1013
 1014

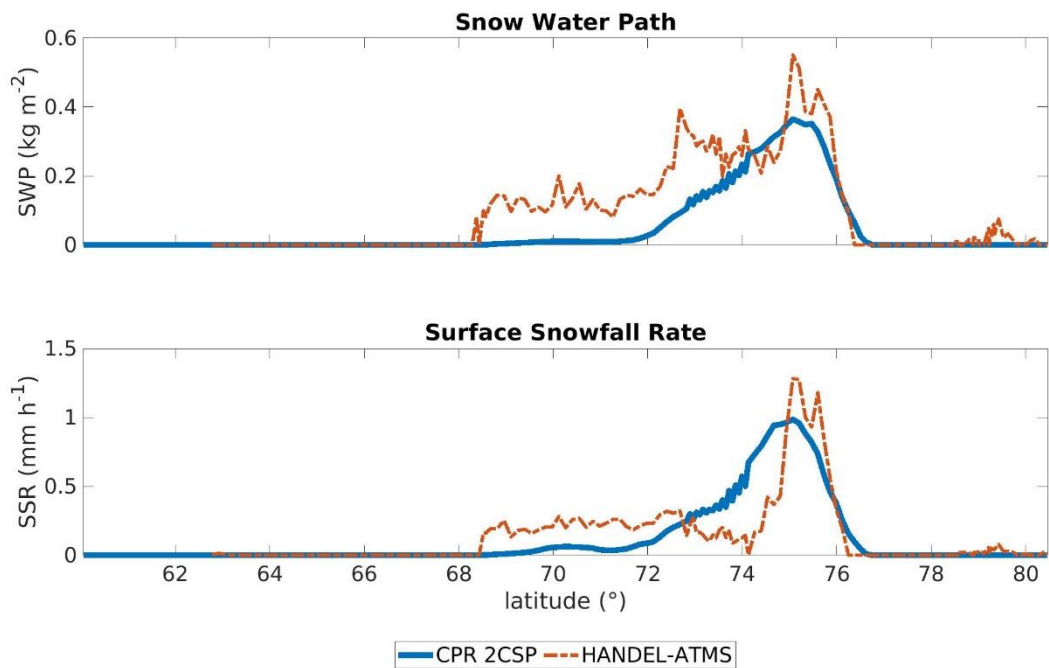
Figure 1516: Greenland - 2016/04/24 - Maps of the HANDEL-ATMS module's output: the SWP detection mask (top panel), the estimated SWP (kg m^{-2}) (second panel), the SSR detection mask (third panel), the estimated SSR (mm h^{-1}) (bottom panel). The green dotted lines (bottom panel) represent the CloudSat track.

1015
1016



1017

1018



1019

1020

1021

1022

1023

1024

1025

1026

Tables

Figure 1617: Greenland - 2016/04/24 - Comparison between CPR 2C-SNOW-PROFILE and HANDEL-ATMS SWP and SSR estimates along the CloudSat track.

1027
1028

	OCEAN MODULE	LAND MODULE
POD	0.99	0.98
FAR	0.01	0.01
HSS	0.98	0.72

1029
1030
1031
1032
1033
1034
1035
1036
1037
1038
1039
1040
1041
1042
1043
1044

Table 1: PESCA Overall Statistical Scores.

<u>Class</u>	<u>TPW (mm)</u>	<u>T_{2m} (K)</u>	<u># obs</u>	<u>% SWP obs</u>	<u>% SSR obs</u>	<u>SWP (kg m⁻²)</u>	<u>SSR (mm h⁻¹)</u>
<u>Ocean</u>	<u>6.2</u>	<u>273</u>	<u>3.9*10⁵</u>	<u>79</u>	<u>64</u>	<u>0.046</u>	<u>0.071</u>
<u>New Sea Ice</u>	<u>3.2</u>	<u>255</u>	<u>2.1*10⁵</u>	<u>38</u>	<u>38</u>	<u>0.033</u>	<u>0.050</u>
<u>Broken Sea Ice</u>	<u>5.2</u>	<u>266</u>	<u>1.4*10⁵</u>	<u>57</u>	<u>57</u>	<u>0.044</u>	<u>0.073</u>
<u>Multilayer Sea Ice</u>	<u>4.5</u>	<u>260</u>	<u>9.9*10⁴</u>	<u>43</u>	<u>43</u>	<u>0.033</u>	<u>0.051</u>
<u>Land</u>	<u>5.3</u>	<u>270</u>	<u>2.8*10⁴</u>	<u>43</u>	<u>41</u>	<u>0.043</u>	<u>0.068</u>
<u>Perennial Snow</u>	<u>1.6</u>	<u>248</u>	<u>3.6*10⁵</u>	<u>31</u>	<u>31</u>	<u>0.022</u>	<u>0.035</u>
<u>Winter Polar Snow</u>	<u>2.1</u>	<u>245</u>	<u>6.0*10⁴</u>	<u>32</u>	<u>32</u>	<u>0.033</u>	<u>0.048</u>
<u>Deep Dry Snow</u>	<u>3.8</u>	<u>261</u>	<u>1.1*10⁵</u>	<u>50</u>	<u>50</u>	<u>0.040</u>	<u>0.066</u>
<u>Thin Snow</u>	<u>4.5</u>	<u>267</u>	<u>1.8*10⁴</u>	<u>54</u>	<u>53</u>	<u>0.041</u>	<u>0.070</u>
<u>Coast</u>	<u>4.0</u>	<u>259</u>	<u>3.1*10⁵</u>	<u>47</u>	<u>46</u>	<u>0.043</u>	<u>0.068</u>

1045
1046
1047

Table 2: Environmental Characteristics for each PESCA class (test dataset): the number of occurrences, the mean TPW and T_{2m} value, the percentage of SWP/SSR observations (over the total occurrences) and the mean SWP and SSR values are shown.

Class	n clusters	accuracy	165.5 GHz RMSE (K)	165.5 GHz NRMSE%	Predictor Set
Ocean	2	0.9	3.37	44	P _{surf} - TPW - T _{2m}

New Sea Ice	3	0.74	4.52	48	SI - T _{2m} - P _{surf} - ratio - jd - pem ₂₃
Broken Sea Ice	16	0.56	5.34	41	pem ₂₃ - TPW - SI - P _{surf}
Multilayer Sea Ice	9	0.53	4.38	34	pem ₃₁ - SI - TPW - T _{2m} - pem ₂₃ - P _{surf}
Land	2	0.87	4.57	52	DEM - jd - TPW
Perennial Snow	8	0.65	5.98	54	pem ₂₃ - jd - SI - pem ₃₁ - lat
Winter Polar Snow	5	0.76	5.87	37	pem ₃₁ -SI - lat -H _{sol} - pem ₃₁ - jd
Deep Dry Snow	15	0.34	6.77	45	SI - pem ₃₁ - ratio
Thin Snow	3	0.78	6.03	39	SI -ratio - lat
Coast	13	0.43	6.80	44	SI - pem ₂₃ - pem ₃₁ - DEM - T _{2m}

1048 **Table 23: Classification Refinement - Parameters.**

1049
1050
1051
1052
1053
1054

Predictor Set	POD	FAR	HSS
$\Delta TB_{obs-sim} +$ ancillary parameters	0.75	0.29	0.48
TB _{obs} + ancillary parameters	0.81	0.18	0.65
TB _{obs} + environmental var + ancillary parameters	0.82	0.17	0.68
TB _{obs} + $\Delta TB_{obs-sim} +$ ancillary parameters	0.84	0.16	0.69

1055 **Table 34: HANDEL-ATMS SSR Detection Performance: Statistical scores for different Predictor Sets. The statistical**
1056 **scores have been calculated for the test dataset.**

1057
1058

	POD	FAR	HSS
SWP	0.85	0.15	0.70
SSR	0.84	0.16	0.69

1059 **Table 45: HANDEL-ATMS detection Performance - SWP and SSR Detection Modules Statistical Scores. The statistical**
1060 **scores have been calculated for the test dataset.**

1061
1062

	RMSE	bias	R ²
SWP (kg m ⁻²)	0.047	0.001	0.72
SSR (mm h ⁻¹)	0.079	0.002	0.61

1063 **Table 56: HANDEL-ATMS Estimation Performance - SWP and SSR Estimation Module Error Statistics. The error**
1064 **statistics have been calculated for the test dataset.**

1065
1066

	POD		FAR	
	SLALOM-CT	HANDEL-ATMS	SLALOM-CT	HANDEL-ATMS
TPW<10 mm T _{2m} <280 K (*)	0.82	0.84	0.19	0.16
TPW<5 mm T _{2m} <250 K	0.64	0.68	0.28	0.23
TPW<3 mm T _{2m} <240 K	0.45	0.54	0.33	0.28

1067 **Table 67:** Comparison between HANDEL-ATMS and SLALOM-CT detection Performances for Different
1068 Environmental Conditions (* HANDEL-ATMS working limits).